Dendrify: a new framework for seamless incorporation of dendrites in Spiking Neural Networks

Michalis Pagkalos[1,2], Spyridon Chavlis[1], Panayiota Poirazi[1,*]

[1] *Institute of Molecular Biology and Biotechnology (IMBB), Foundation for Research and Technology Hellas (FORTH), Heraklion, 70013, Greece*

[2] *Department of Biology, University of Crete, Heraklion, 70013, Greece*

[*] *Corresponding author: poirazi@imbb.forth.gr*

Abstract

Computational modeling has been indispensable for understanding how subcellular neuronal features influence circuit processing. However, the role of dendritic computations in network-level operations remains largely unexplored. This is partly because existing tools do not allow the development of realistic and efficient network models that account for dendrites. Current spiking neural networks, although efficient, are usually quite simplistic, overlooking essential dendritic properties. Conversely, circuit models with morphologically detailed neuron models are computationally costly, thus impractical for large-network simulations. To bridge the gap between these two extremes, we introduce *Dendrify*, an open-source Python package compatible with *Brian2,* designed to facilitate the development of bioinspired spiking neural networks. *Dendrify*, through simple commands, automatically generates reduced compartmental neuron models with simplified yet biologically relevant dendritic and synaptic integrative

properties. Such models strike a good balance between flexibility, performance, and biological accuracy, allowing us to explore dendritic contributions to network-level functions while paving the way for developing more powerful neuromorphic systems.

Introduction

Simulations of spiking neural networks (SNNs) are widely used to understand how brain functions arise from area-specific network dynamics[1]. Moreover, SNNs have recently gained much attention for their value in low-power neuromorphic computing and practical machine learning applications[2,3]. SNNs typically comprise point, integrate-and-fire (I&F) neurons and can replicate basic biological features such as specific connectivity motifs, excitation-inhibition dynamics, and learning via synaptic plasticity rules. However, SNNs often ignore dendrites, the thin membranous extensions of neurons that receive the vast majority of incoming inputs. Numerous studies have shown that the dendrites of excitatory and inhibitory neurons possess compelling computational capabilities[4,5] that can significantly influence both neuronal and circuit function[6–9] and cannot be captured by point-neuron SNNs.

First, dendrites can act as semi-independent thresholding units, producing local regenerative events termed dendritic spikes (dSpikes). These spikes are generated by local voltage-gated mechanisms (e.g., Na^+/Ca^{2+} channels, NMDA receptors) and influence both synaptic input integration and plasticity[4,5]. Moreover, dendritic mechanisms operate in multiple timescales, ranging from a few up to hundreds of milliseconds, allowing complex computations, including coincidence detection, low-pass filtering, input segregation/amplification, parallel nonlinear processing, and logical operations[10–15].

Due to these nonlinear phenomena, the arrangement of synapses along dendrites becomes a key determinant of local and somatic responses. For example, the impact of inhibitory pathways depends on their exact location relative to excitatory inputs[16,17]. Moreover, functionally related synapses can form anatomical clusters, which facilitate the induction of dSpikes, thus increasing computational efficiency and storage capacity[18–20]. Finally, dendritic morphology and passive properties shape the general electrotonic properties of neurons[4]. For example, dendritic filtering affects both the amplitude and the kinetics of synaptic currents traveling towards the soma in a location-dependent manner. Given the complexity of dendritic processing, SNNs that lack dendrites may fail to account for important dendritic contributions to neuronal integration and output, limiting their true computational power.

Conversely, biophysical models of neurons with a detailed morphology are ideal for studying how dendritic processing affects neuronal computations at the single-cell level[1]. Such models comprise hundreds of compartments, each furnished with numerous ionic mechanisms to faithfully replicate the electrophysiological profile of simulated neurons. However, achieving high model accuracy is typically accompanied by increased complexity (e.g., higher CPU/GPU demands and larger run times), as numerous differential equations have to be solved at each simulation time step[1]. Therefore, this category of models is unsuitable for large-network simulations, where computational efficiency is a key priority.

A middle-ground solution utilizes simplified models that capture only the essential electrophysiological characteristics of real neurons[21–26]. Notable examples of this approach are found in recent theoretical studies showing that dendritic mechanisms convey significant advantages to simplified network models of varying levels of abstraction. These include improved

63 associative learning[20], better input discrimination (pattern separation[27]), efficient short-term
64 memory (persistent activity[28]), and increased memory storage and recall capacity[8]. Similar
65 advantages were recently seen in the machine learning field: the addition of dendritic nodes in
66 artificial neural networks (ANNs) reduced the number of trainable parameters required to
67 achieve high-performance accuracy[29] (also see[30]). Moreover, incorporating dendritic nodes in
68 Self Organizing Map classifiers[31] and other types of neuro-inspired networks[32] improved their
69 ability to learn continuously.

70 Overall, while dendrites confer advanced computational power to simulated biological
71 networks and these benefits are likely to extend to machine learning systems, SNNs remain
72 largely dendrite-ignorant. A likely reason is that the current theoretical framework for modeling
73 dendritic properties consists of overly complex equations with numerous free parameters,
74 making it mathematically intractable and impractical for use in SNNs.

75 To address the abovementioned complexity issues and provide a framework that allows
76 the seamless incorporation of dendrites in SNN models, we developed *Dendrify* (**Figure 1**).
77 *Dendrify* is a free, open-source *Python* package that facilitates the addition of dendrites along
78 with various dendritic mechanisms in SNNs. Importantly, *Dendrify* works seamlessly with the
79 *Brian 2* simulator[33]; it builds upon the powerful and flexible features of the latter while it
80 automates some potentially complex and error-prone steps related to compartmental modeling.
81 Specifically, through simple and intuitive commands, *Dendrify* automatically generates and
82 handles all the equations (and most parameters) needed by *Brian 2* to build simplified
83 compartmental neurons. Its internal library of premade models supports a broad range of
84 neuronal mechanisms, yet it allows users to provide their own model equations. Among other

85 optimizations, we also introduce a novel phenomenological approach for modeling dSpikes,

86 significantly more efficient and mathematically tractable than the Hodgkin-Huxley formalism.

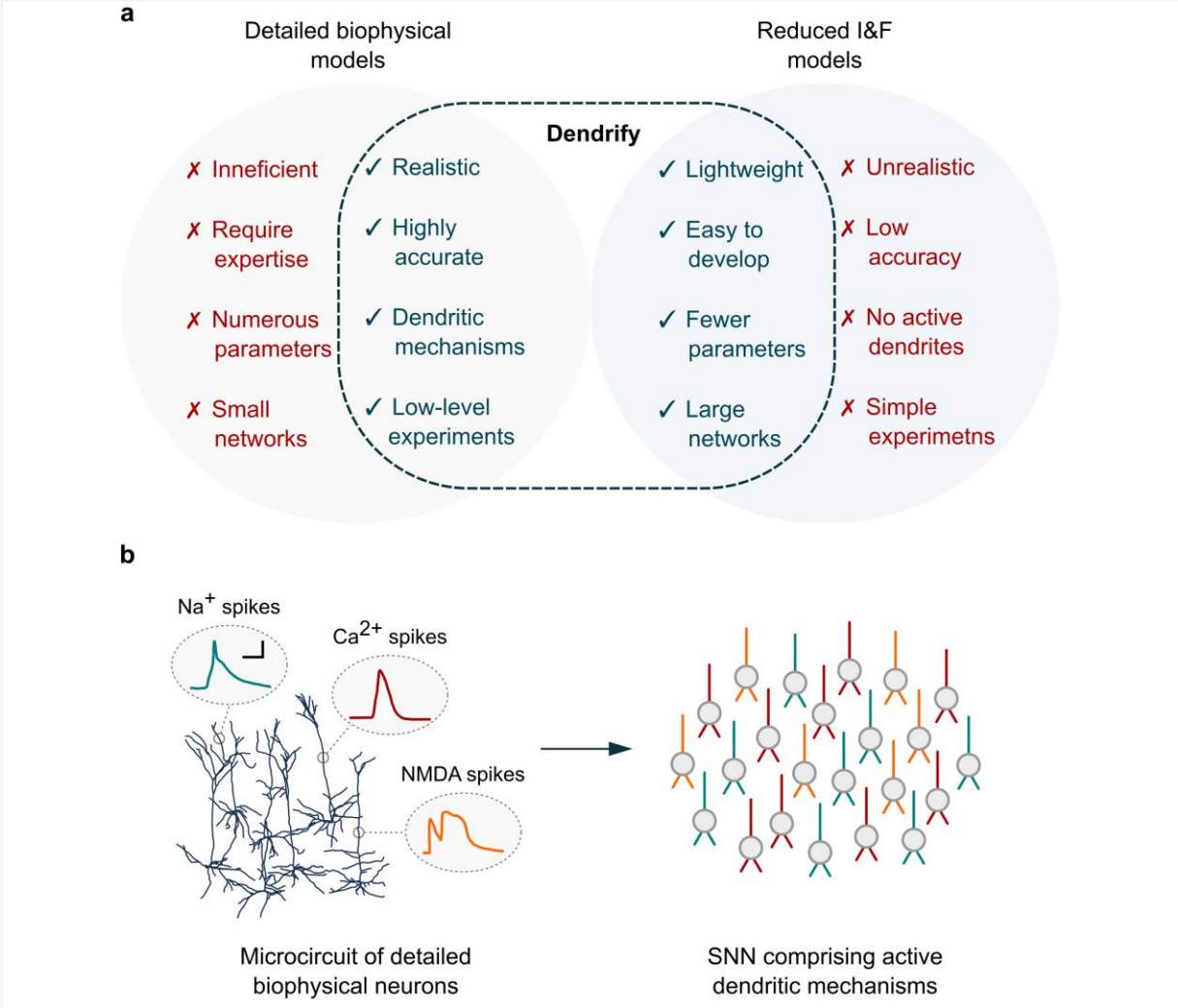

Figure 1 | The main characteristics of *Dendrify*. a) *Dendrify* stemmed from our efforts to bridge the gap between detailed biophysical models and reduced I&F models. The result is a modeling framework for developing simplified compartmental models that balance efficiency and biological accuracy by capturing the most important characteristics of both worlds. **b)** *Dendrify* facilitates the development of SNNs comprising reduced compartmental neurons (ball and sticks) and known dendritic phenomena, such as various types of local spikes (Color code; teal: Na^+ spikes, red: Ca^{2+} spikes, orange: NMDA spikes. Scalebar: 20mV / 10ms).

87 To demonstrate the power of *Dendrify*, we showcase its main features through four
88 modeling paradigms of increasing complexity. a) A basic compartmental model with passive
89 dendrites, b) a reduced compartmental model with active dendrites, c) a simplified model of a
90 CA1 pyramidal neuron that reproduces numerous experimental observations, and d) a pool of
91 CA1 neurons used to assess the contribution of dendritic Na^+ spikes in coincidence input
92 detection. Moreover, we provide a step-by-step guide for designing reduced compartmental
93 models that capture the key electrophysiological and anatomical properties of their biological
94 counterparts. Notably, the proposed guide builds upon established theoretical work[21,22,24], and
95 its implementation is not exclusive to any simulator software. To our knowledge, this is the first
96 tool that adds dendrites to simple, phenomenological neuronal models in a standardized and
97 mathematically concise manner.

98 # Results

99 ## Example 1: A basic compartmental model with passive dendrites

100 We start with a simple neuron model consisting of three compartments (**Fig. 2a**). A soma,
101 modeled as a leaky I&F unit, and two passive dendrites (apical & basal) that are electrically
102 coupled to the soma (see Methods). This architecture is meant to roughly resemble the general
103 dendritic organization of excitatory, pyramidal-like neurons. In this example, the apical dendrite
104 can integrate excitatory synaptic inputs consisting of a fast α-amino-3-hydroxy-5-methyl-4-
105 isoxazolepropionic acid (AMPA) component and a slow N-methyl-D-aspartate (NMDA)
106 component. In addition, both dendritic compartments are connected to a source of Gaussian

107 white noise (i.e., noisy input current). The *Python* code needed to reproduce this model is

108 described in **Fig. 3**. All model parameters are available in **Table S1**.

109 To test our model's electrical behavior, we applied depolarizing current injections (400 ms

110 pulses of 100 pA at -70 mV baseline voltage) individually to each compartment and recorded the

111 voltage responses of all compartments (**Fig. 2b**). As expected, the largest depolarization was

112 observed at the current injection site, while compartments located further apart were less

113 affected. Note that the basal dendrite in this model is more excitable than the apical one due to

114 the difference in length (150 µm vs. 250 µm, respectively). The attenuation of currents traveling

115 along the somatodendritic axis is an intrinsic property of biological neurons and is due to the

116 morphology and cable properties of dendritic trees[4,34].

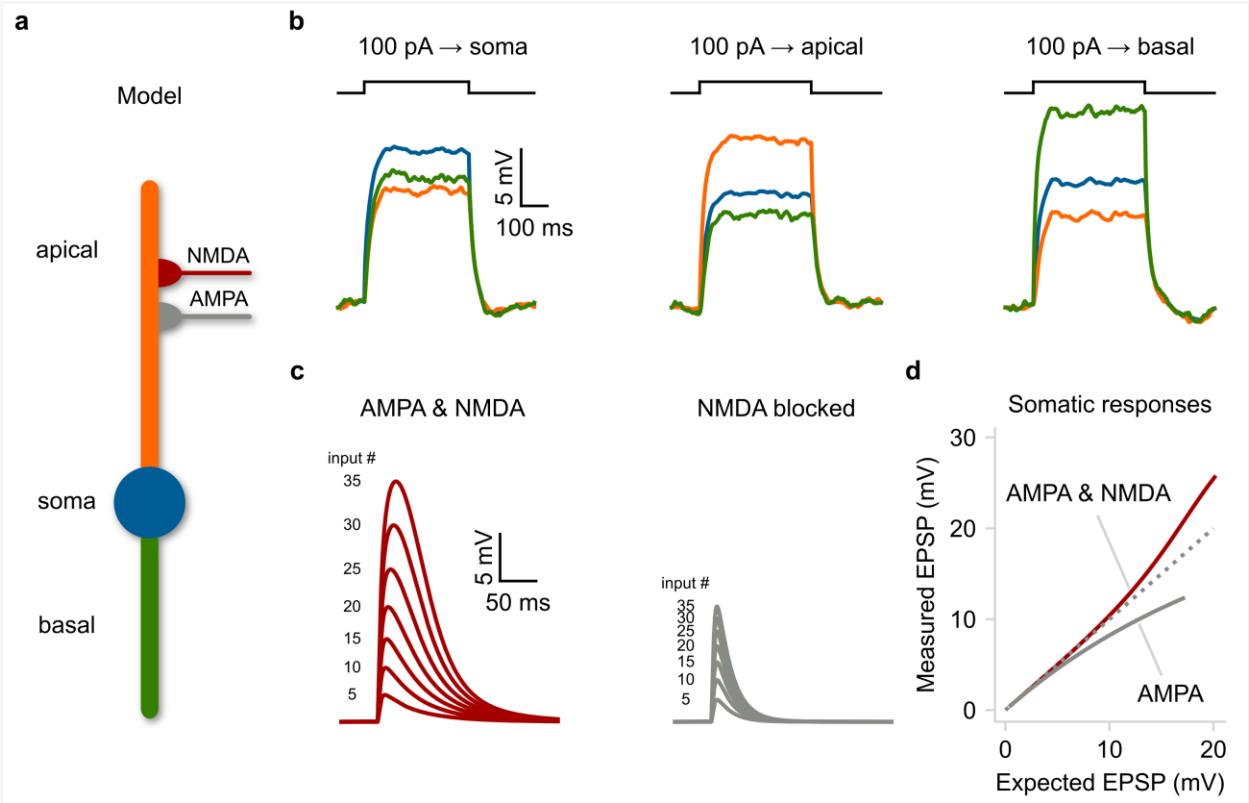

Figure 2 | A basic compartmental neuron model with passive dendrites. a) Schematic

illustration of a compartmental model consisting of a soma (spiking unit) and two dendrites (passive integrators). The apical dendrite can integrate excitatory synapses comprising AMPA and NMDA currents. **b)** Membrane voltage responses to current injections of the same amplitude, applied individually to each compartment. Notice the electrical segregation caused by the resistance between the three neuronal compartments. **c)** Somatic responses to a varying number of simultaneous synaptic inputs. Left: control EPSPs, right: EPSPs in the presence of NMDA blockers. **d)** Input-output function of the apical dendrite as recorded at the soma. The dotted line represents a linear function. Notice the shift from supralinear to sublinear mode when NMDARs are blocked. The simulations and analysis code related to the above figure will be provided upon reasonable request, and will be freely available upon publication.

117 Although dendritic attenuation may seem undesirable, it has several computational
118 advantages[4]. For instance, it allows dendrites to operate semi-independently from the soma[35]
119 and perform complex functions, especially when paired with local voltage-gated mechanisms. In
120 our toy model, simultaneous activation of an increasing number of synapses on the apical
121 dendrite evokes somatic responses much larger than the expected arithmetic sum of individual
122 inputs (**Fig. 2c-d**). The additional depolarization is due to the activation of NMDARs (at elevated
123 dendritic voltages), resulting in supralinear integration. However, when NMDARs are blocked,
124 the apical dendrite switches from supralinear to a sublinear integration mode (**Fig. 2c-d**), and this
125 alteration can be dendrite-specific. This happens because synaptic currents are susceptible to the
126 decrease in driving force as dendritic voltage approaches the AMPA reversal potential (E_{AMPA} = 0
127 mV). Both types of dendritic integration have been observed in real neurons and allow distinct
128 computations, such as e.g. clustered vs. scattered input sensitivity[34].

129 This example shows that even rudimentary compartmental models can simulate essential

dendritic functions like signal attenuation and segregation that point-neuron models cannot capture. Importantly, they allow the presence of multiple input segregation sites, theoretically enhancing the computational capacity of single neurons[36]. In addition, we provide an example of how even basic dendritic-driven mechanisms can impact neuronal integration and somatic output.

```
1  import brian2 as b
2  from brian2.units import *
3  from dendrify import Soma, Dendrite, NeuronModel
4
5  # create soma
6  soma = Soma('soma', model='leakyIF', length=25*um, diameter=25*um)
7
8  # create apical dendrite
9  apical = Dendrite('apical', length=250*um, diameter=2*um)
10
11 # create basal dendrite
12 basal = Dendrite('basal', length=150*um, diameter=2*um)
13
14 # add noise to dendrites
15 apical.noise(tau=20*ms, sigma=3*pA, mean=0*pA)
16 basal.noise(tau=20*ms, sigma=3*pA, mean=0*pA)
17
18 # add synapses
19 apical.synapse('AMPA', pre='cortex', g=1*nS, t_decay=2*ms)
20 apical.synapse('NMDA', pre='cortex', g=1*nS, t_decay=60*ms)
21
22 # merge the compartments into a NeuronModel and set its basic properties
23 edges = [(soma, apical, 10*nS), (soma, basal, 10*nS)]
24 pyr_model = NeuronModel(edges, cm=1*uF/(cm**2), gl=50*uS/(cm**2),
25                          v_rest=-70*mV, r_axial=150*ohm*cm,
26                          scale_factor=3, spine_factor=1.5)
27
28 # create a Brian NeuronGroup and link it to the NeuronModel
29 pyr_group = b.NeuronGroup(4, model=pyr_model.equations, method='euler',
30                          threshold='V_soma > -40*mV', reset='V_soma = -50*mV',
31                          refractory=3*ms, namespace=pyr_model.parameters)
32 pyr_model.link(pyr_group)
```

Figure 3 | Python code for the neuron model in Figure 2a. *Dendrify* applies a standardized approach for describing the architecture, mechanisms, and parameters of simplified compartmental models. This approach involves creating *Soma/Dendrite* objects (lines 6, 9, 12)

representing the model's compartments. Here, soma acts as the primary spiking unit (leaky I&F), while dendrites are simulated (by default) as passive leaky integrators. Users can specify each compartment's physical dimensions, which are used to calculate its surface area. Moreover, *Dendrify* allows adding any desired mechanism (dendritic, synaptic, or other) to a single compartment, such as Gaussian noise (lines 15, 16) and synaptic currents (lines 19, 20). Users can specify the coupling strength between the adjacent compartments (line 23); otherwise, it is inferred from the model parameters (see Methods). Finally, we introduce another object, the *NeuronModel* (line 24), which has four primary functions: a) to group related *Compartment* objects into a single model, b) to allow setting global model parameters, c) to extract model equations, properties, and custom events, d) to allow deeper integration with *Brian 2,* which unlocks several automations (line 32). Upon creating a *NeuronModel*, users can easily construct a *NeuronGroup* (line 29 - a group of neurons that share the same equations and properties), *Brian's* core object of every simulation. The entire simulation code and detailed *Dendrify* examples will be freely available on *GitHub*. For more information, see the Methods section and the *Brian 2* documentation: https://brian2.readthedocs.io/en/stable.

Example 2: A reduced compartmental model with active dendrites

In the previous example, dendrites were modeled as passive leaky compartments with added synaptic mechanisms. However, a unique feature of *Dendrify* is the ability to incorporate voltage-gated ion channels (VGICs, see Methods) that are implemented phenomenologically without utilizing the Hodgkin-Huxley formalism. This approach further reduces mathematical and computational complexity as exemplified by a second reduced model (parameters shown in **Table S2**) consisting of a somatic compartment (leaky I&F) and an apical dendrite divided into three segments (**Fig. 4a, Fig. 5**). All dendritic compartments are equipped with models of Na^+-type VGICs (allowing the generation of Na^+ dSpikes), while the distal and proximal segments can

144 integrate synaptic inputs consisting of AMPA and NMDA currents.

145 First, to test the impact of locally generated Na^+ spikes on dendritic and somatic responses
146 in the model neuron, we simulated the application of short current injections (5 ms long pulses
147 of rheobase intensity) to each dendritic segment and recorded simultaneously from all
148 compartments (**Fig. 4b-d**). Although model parameters were adjusted to elicit nearly identical
149 responses in all dendritic compartments (**Fig. 4e** left), somatic responses varied significantly,
150 depending on the dSpike initiation site (**Fig. 4e** right). As in real neurons, distal dSpikes became
151 much weaker and broader as they traveled towards the soma due to the dendritic filtering
152 effect[4,37].

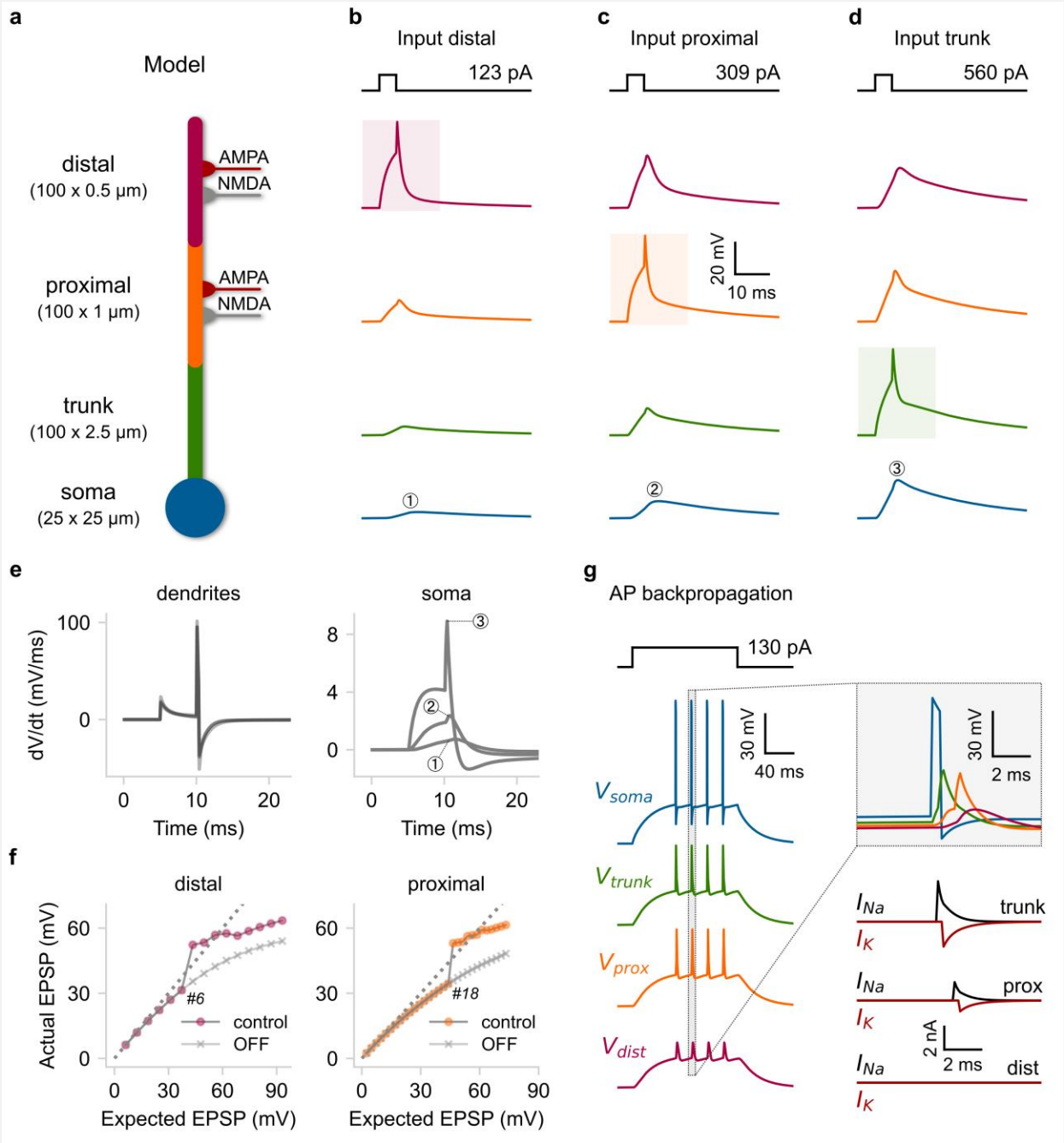

Figure 4 | A reduced compartmental model that replicates active dendritic properties. a) Schematic illustration of a compartmental model consisting of a soma (leaky I&F) and three dendritic segments (trunk, proximal, distal) equipped with Na^+-type VGICs. The distal and proximal segments can also receive AMPA and NMDA synapses. **b-d)** Rheobase current injections (5ms square pulses) for dSpike generation were applied individually to each dendritic segment.

Shaded areas: location of current injection and dSpike initiation. Top: stimulation protocol showing the current threshold for a single dSpike (rheobase current). **e)** First temporal derivative of dendritic (left) and somatic (right) voltage traces from panels b-d. **f)** Input-output function of the distal (left) and proximal (right) segment as recorded from the corresponding dendritic locations. We also indicate the number of quasi-simultaneously activated synapses (ISI = 0.1 ms) needed to elicit a single dSpike in each case. OFF: deactivation of Na^+ dSpikes. Dashed lines: linear input-output relationship. **g)** Left: Backpropagating dSpikes are generated in response to somatic current injections. The short-amplitude spikelets detected in the distal branch are subthreshold voltage responses for dSpike initiation. Right: Magnified and superimposed voltage traces (top) from the dashed box (left). Bellow: dendritic voltage-activated currents responsible for dSpikes generation in each dendritic segment. The simulations and analysis code related to the above figure will be provided upon reasonable request, and will be freely available upon publication.

153 Moreover, the threshold for dendritic spiking significantly differs among the three dendritic
154 locations (**Fig. 4b-d top**). For example, dSpike generation in the distal segment (**Fig. 4b**) requires
155 approximately 2.5 times less current than the proximal one (**Fig. 4c**). Due to its smaller diameter
156 and sealed end, the distal segment has higher input resistance (Rinput); thus, its membrane is
157 more excitable. Biological neurons also exhibit a large variability of axial resistance along their
158 dendrites caused mainly by differences in local branch dimensions (length and diameter) and
159 dendritic geometry (e.g., bifurcations number, branch order). This location-dependent change in
160 input resistance (typically increases in the thinner, distal branches) serves two functions. First, it
161 increases the probability of dSpike initiation in the distal dendritic branches, and second, it helps
162 to counterbalance the distance-dependent input attenuation caused by cable filtering[34,37,38].

163 To examine how dendritic spiking combined with local branch properties affect synaptic

164 integration in our toy model, we activated quasi-simultaneously (train of spikes with ISI 0.1 ms)
165 an increasing number of synapses placed on the distal and the proximal segments. We then
166 compared the peak amplitude of the dendritic voltage responses (Actual) to what would be
167 obtained by a linear arithmetic sum of unitary responses (Expected) (**Fig. 4f**). Both segments
168 produce voltage responses that increase in a sigmoid-like fashion, with a supralinear rise in their
169 amplitude occurring above a certain number of synapses (**Fig. 4f** control). This behavior is typical
170 of pyramidal neurons in the cortex and the hippocampus[10,12,35,39] as well as some
171 interneurons[7,40]. Moreover, blocking dSpikes (**Fig. 4f** OFF) disrupts the above response leading to
172 sublinear integration. Although the two segments appear to have similar input-output curves,
173 dendritic nonlinearities emerge earlier in the distal compartment. This is because of its higher
174 input resistance (R_{input}), requiring less synaptic excitation to cross the dSpike voltage threshold.
175 This model property, which is based on experimental data[37], highlights the importance of
176 accounting for input pathways projecting to different dendritic locations, as they may be subject
177 to different integration rules. Notably, the same approach used to build phenomenological
178 models of Na^+ dSpikes can be used to build models of other types of local spikes (e.g., Ca^{2+}-based).

179 Another key feature of biological neurons is the ability of APs initiated in the axon to invade
180 the soma and nearby dendrites and propagate backward towards the dendritic tips. The
181 transmission efficacy of these backpropagating action potentials (BPAPs) depends on the
182 dendritic morphology and the abundance of dendritic VGICs (Na^+ or Ca^{2+})[36]. Notably, in several
183 neuronal types, BPAPs can propagate more efficiently than forward-propagating dSpikes, acting
184 as feedback signals of somatic activity[36] and serving as instructive plasticity signals[41–43]. To test if
185 our model can recreate the generation of BPAPs, we injected a depolarizing step current at the

186 soma (135 pA for 300 ms) capable of eliciting a small number of somatic APs (**Fig. 4f**). Upon
187 somatic activation (the axon is not explicitly modeled here), BPAPs were successfully generated
188 and propagated to the distal dendritic segment. There, dSpikes were reduced to sharp, small-
189 amplitude responses (spikelets), as observed experimentally[44]. These spikelets resulted from
190 attenuating ion influxes from nearby dSpikes, that failed to trigger local suprathreshold
191 responses. It should be noted that to achieve BPAP generation, we had to utilize a custom version
192 of the I&F model[20] that results in a more realistic somatic AP shape (see Methods).

193 Altogether, the above simulations show that *Dendrify* allows the development of reduced
194 compartmental models that incorporate phenomenological voltage-gated mechanisms and can
195 replicate a variety of dendritic features and their impact on somatic output. These reduced yet
196 more biologically relevant models offer a compelling alternative for developing SNNs with a high
197 degree of bioinspiration and small computational overhead. Importantly, *Dendrify* provides easy
198 access to this category of models by radically simplifying their implementation in *Brian 2.*

199 Example 3: A simplified yet biologically accurate model of a CA1 pyramidal cell

200 The previous examples demonstrated how *Dendrify* promotes the development of simple
201 compartmental models reproducing several essential dendritic functions. However, our
202 examples comprised generic neuron models rather than an area-specific cell type. To explore our
203 approach's full potential and limitations, we built a simplified yet realistic model of a CA1
204 pyramidal cell (PC). This cell type was selected due to the availability of a large number of
205 experimental data[45] and computational models[46,47] to compare our work with. Notably, to keep

206 our approach simple, we did not use third-party software to design the model's morphology[48] or
207 fit its parameters[49]. Instead, based on previous theoretical work[21,22,24], we created a set of
208 instructions that guides *Dendrify* users throughout model development and validation processes.
209 The specific approach is briefly discussed below (for a more detailed description, see Methods).

210 Our reduced CA1 PC model (**Fig. 6a**) consists of 9 segments (1 somatic + 8 dendritic), the
211 dimensions of which were constrained using mouse anatomical data[50,51]. All model parameters
212 are provided in **Table S3**. Our goal was to preserve: a) the main functional and anatomical
213 characteristics of the dendritic morphology, b) accurate synaptic placement, and c) realistic
214 dendritic attenuation (axial resistance). In particular, this morphology reflects the anatomical
215 layering of the CA1 hippocampal area and the spatial segregation of input pathways coming from
216 the Entorhinal Cortex (EC) and the CA3 area, respectively. Moreover, synaptic conductances were
217 manually calibrated to ensure that the AMPA to NMDA ratio and the unitary postsynaptic
218 responses along the dendritic tree agree with empirical data (**Fig. S2**, **Table S3**)[52–57]. To directly
219 compare our model with the available *in vitro* data[45], we replicated the experimental procedures
220 used to estimate essential electrophysiological properties (**Fig. 6b-c**, **Fig. S1**). We observe that
221 the model's membrane time constant (τ_m), input resistance (R_{input}), sag ratio, and F-I curve closely
222 approximate the respective properties of real PCs located in the CA1b subregion, the most central
223 part of the CA1 area.

```
1  import brian2 as b
2  from brian2.units import *
3  from dendrify import Soma, Dendrite, NeuronModel
4
5  # create soma
6  soma = Soma('soma', model='leakyIF', length=25*um, diameter=25*um )
7
8  # create trunk
9  trunk = Dendrite('trunk', length=100*um, diameter=2.5*um)
10 trunk.dspikes('Na', threshold=-35*mV, g_rise=34*nS, g_fall=27.2*nS)
11
12 # create proximal dendrite
13 prox = Dendrite('prox', length=100*um, diameter=1*um)
14 prox.synapse('AMPA', pre='pathY', g=0.8*nS,  t_decay=2*ms)
15 prox.synapse('NMDA', pre='pathY', g=0.8*nS,  t_decay=60*ms)
16 prox.dspikes('Na', threshold=-35*mV, g_rise=15.3*nS, g_fall=12.24*nS)
17
18 # create distal dendrite
19 dist = Dendrite('dist', length=100*um, diameter=0.5*um)
20 dist.synapse('AMPA', pre='pathX', g=0.8*nS,  t_decay=2*ms)
21 dist.synapse('NMDA', pre='pathX', g=0.8*nS,  t_decay=60*ms)
22 dist.dspikes('Na', threshold=-35*mV, g_rise=7*nS, g_fall=5.6*nS)
23
24 # merge the compartments into a NeuronModel and set its basic properties
25 edges = [(soma, trunk, 15*nS), (trunk, prox, 10*nS), (prox, dist, 4*nS)]
26 pyr_model = NeuronModel(edges, cm=1*uF/(cm**2), gl=40*uS/(cm**2),
27                        v_rest=-70*mV, r_axial=150*ohm*cm,
28                        scale_factor=2.8, spine_factor=1.5)
29
30 # set dSpike properties
31 pyr_model.dspike_properties('Na', tau_rise=0.6*ms, tau_fall=1.2*ms,
32                            refractory=5*ms, offset_fall=0.2*ms)
33
34 # create a Brian NeuronGroup and link it to the NeuronModel
35 pyr_group = b.NeuronGroup(1, model=pyr_model.equations, method='euler',
36                          threshold='V_soma > -40*mV', reset='V_soma = 40*mV',
37                          refractory=4*ms, events=pyr_model.events,
38                          namespace=pyr_model.parameters)
39 pyr_model.link(pyr_group)
```

Figure 5 | Python code for the model shown in Figure 4a. The code shown here follows the same principles described in **Fig. 3**. In addition, we introduce another feature of *Dendrify,* which is the option to add a dendritic spiking mechanism to *Dendrite* objects (lines 10, 16, 22). Dendritic spiking is modeled in an event-driven fashion, which mimics the rising and falling phase of dSpikes caused by the sequential activation of inward Na^+ (or Ca^{2+}) and outward K^+ currents (**Fig. 4g**, also see Methods). Users can specify the dSpike threshold and the amplitudes of the inward ('g_rise') and outward ('g_fall') currents individually in each dendrite. Moreover, it is possible to set global dSpike properties (lines 31, 32), such as the decay time constants for the rise and the fall phases,

the temporal delay of the fall phase (offset_fall), and a dSpike refractory period.

224 Since studies with simultaneous somatodendritic recordings are scarce in the literature, we
225 utilized data from various sources (experimental[39,52] and modelling[35,46,47,58]) to calibrate our
226 model's dendritic properties. First, to quantify dendritic attenuation as a function of distance
227 from the soma, we injected current at the soma (1,000 ms square pulse of -10 pA) and calculated
228 the ratio of the dendritic to somatic steady-state voltage responses (dV_{dend}/dV_{soma}) at various
229 locations. The reduced model is similar to three detailed biophysical models[46] (**Fig. 6d**). Next, to
230 examine synaptic input attenuation, we activated synapses (single pulse with a time interval of
231 0.1 ms) at various apical dendrite locations and calculated the somatic to dendritic peak voltage
232 (dV_{soma}/dV_{dend}) (**Fig. 6e**). Compared to experimental data[52] and a recent, highly optimized
233 biophysical model[58], the reduced model captures the distance-dependent attenuation of EPSPs.
234 It should be noted that the high variability in the morphology[51] and the electrophysiological
235 properties[45] of real CA1 PCs make any attempt to build a single (detailed or simplified) neuron
236 model that replicates all characteristics virtually impossible (also see[47]). As an alternative
237 approach, Dendrify's ease of implementation and simulation efficiency allows for the
238 development of multiple, different single neuron models, each designed to replicate specific
239 features found in these cells.

240 The dendrites of biological CA1 PCs express several VGICs that allow them to perform
241 complex operations[1,4,5]. For simplicity, we equipped our CA1 neuron model only with Na^+ VGICs,
242 which underlie the generation of Na^+ dSpikes (**Fig. 4**). First, to test our model's ability to generate
243 BPAPs, we injected current at the soma (500 ms square pulse of 200 pA) and recorded

244 simultaneously from the most distal parts of the apical dendritic segments (**Fig. 4f**). We observed
245 that BPAPs are successfully generated and propagate robustly to the end of the main apical trunk
246 (250 µm from the soma). From that point onwards (> 250 µm from the soma), BPAPs are reduced
247 to small-amplitude spikelets that fail to trigger dSpike initiation in the distal dendritic segments.
248 This phenomenon has also been documented in recent *in vitro* studies[44]. However, we should
249 note that backpropagation efficacy among actual CA1 PCs is quite variable and highly dependent
250 on the dendritic morphology and ionic channel distribution[59].

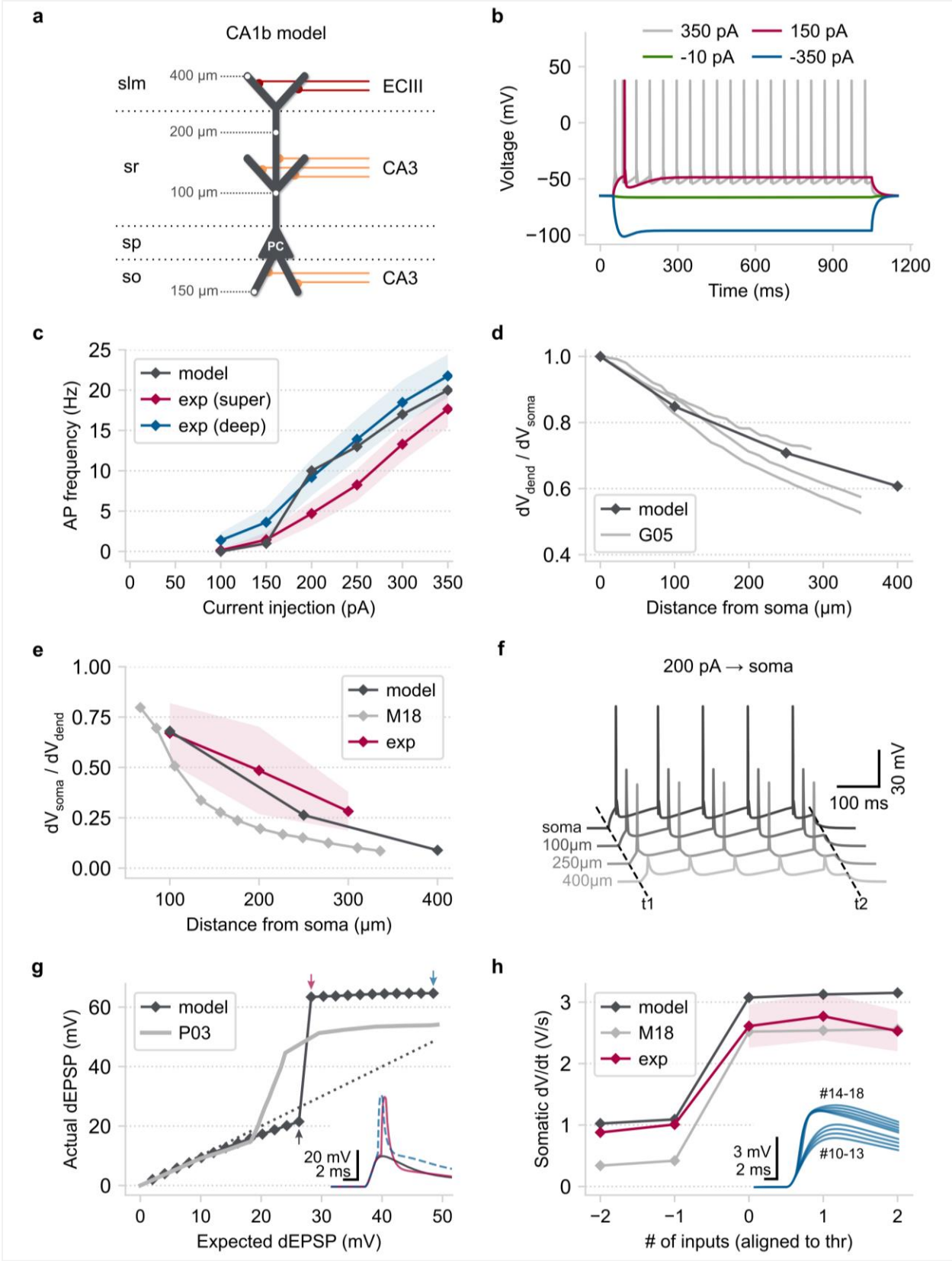
a
CA1b model
slm
400 µm
ECIII
200 µm
sr
CA3
100 µm
sp
PC
so
150 µm
CA3
b
350 pA
150 pA
-10 pA
-350 pA
Voltage (mV)
Time (ms)
c
model
exp (super)
exp (deep)
AP frequency (Hz)
Current injection (pA)
d
model
G05
dV_dend / dV_soma
Distance from soma (µm)
e
model
M18
exp
dV_soma / dV_dend
Distance from soma (µm)
f
200 pA → soma
30 mV
100 ms
soma
100µm
250µm
400µm
t1
t2
g
model
P03
Actual dEPSP (mV)
Expected dEPSP (mV)
20 mV
2 ms
h
model
M18
exp
Somatic dV/dt (V/s)
#14-18
#10-13
3 mV
2 ms
# of inputs (aligned to thr)

Figure 6 | CA1 pyramidal model validation. a) Schematic illustration of our reduced CA1 PC model consisting of a somatic and eight dendritic segments (2 x basal, 1 x proximal trunk, 1 x distal trunk, 2 x radial oblique, 2 x distal tuft). Grey numbers: distance of the indicated points from the soma. Red axons: EC layer two input, orange axons: CA3 input. Long horizontal lines: borders of the four CA1 layers (slm: stratum lacunosum-moleculare, sr: stratum radiatum, sp: stratum pyramidale, so: stratum oriens). **b)** Somatic voltage responses to various (1,000 ms long) current injections used for model validation. **c)** F-I curves comparing the model with actual superficial and deep PCs located in the CA1b area[45]. Shaded area: SEM. **d)** Steady-state, distance-dependent voltage attenuation of a long current pulse injected at the soma. G15: data for three different detailed biophysical models adapted from Golding et al., 2005[46]. **e)** The attenuation of postsynaptic currents propagating along the apical dendrite as a function of distance from the soma. M18: biophysical modeling data adapted from Migliore et al., 2018[58], Exp: experimental data adapted from Magee & Cook, 2000[60]. Shaded area: 2 standard deviations. **f)** Simultaneous somatodendritic recordings in response to a somatic current injection showing the emergence of BPAPs. T1/T2: start/end of current injection (duration = 500 ms). **g)** Main panel: Input-output function of the reduced model's oblique dendrite (the interval between inputs is 0.1 ms). P03: biophysical modeling data adapted from Poirazi et al., 2003[35]. Arrows: indicate a different number of co-active synapses (grey = 13, pink = 14, blue = 24). Inset: dendritic voltage responses from the three highlighted cases. **h)** Main panel: peak dV/dt of somatic voltage responses as a function of synaptic inputs (data aligned to their respective thresholds for dSpike initiation). M18: biophysical modeling data adapted from Migliore et al., 2018[58]. Exp: experimental data adapted from Magee & Cook, 2000[60]. Shaded areas: SEM. Inset: First temporal derivative of the reduced model's somatic EPSPs. Numbers indicate the number of co-active synapses on the apical oblique dendrites. The simulations and analysis code related to the above figure will be provided upon reasonable request, and will be freely available upon publication.

251 Next, we tested our model's ability to generate dSpikes in response to correlated synaptic
252 input onto its oblique dendrites (see **Fig. S3**). This property is a hallmark of real CA1 PCs[39] and

253 was used in the past as a metric of model accuracy[47]. Our model reproduces a sigmoidal-like
254 input-output function (**Fig. 6g**), also observed in a previous example (**Fig. 4f)**. Above a certain
255 number of quasi-simultaneous activation (0.1 ms interval) of synaptic inputs, dendritic responses
256 increase sharply due to dSpike initiation, resulting in supralinear integration[35]. Dendritic sodium
257 spikes cause a rapid jump in the amplitude and kinetics of somatic EPSPs, similar to what is
258 observed in *in vitro* and biophysical modeling studies[39,58] (**Fig. 6h**). Capturing this dendro-somatic
259 nonlinear interaction in our model is essential since this feature is known to increase the
260 conditional excitability of biological CA1 PCs and the temporal precision of their spiking
261 output[5,10].

262 In sum, the above example demonstrates that *Dendrify* can be used to build versatile,
263 reduced models that reproduce a wide range of biophysical and synaptic characteristics of
264 specific types of neurons. Although at a fraction of the computational cost, these reduced models
265 are on par with far more complex ones in terms of accuracy for several features. Moreover, their
266 small number of parameters makes them substantially more flexible and tractable since
267 modelers can easily adjust their properties and incorporate any available data type.

268 Example 4: Pathway interaction in CA1 model neurons

269 Biological CA1 PCs are more likely to generate action potentials when input from the EC on
270 their distal tuft is paired with coincident CA3 input on more proximal dendritic branches. Due to
271 strong dendritic attenuation, distal synaptic input generally has a negligible effect on the soma,
272 even when dSpikes are generated[61]. However, combining EC and (moderate) CA3 input results in
273 more reliable dSpike initiation and propagation, facilitating axonal action-potential output[61].

To test whether our reduced model (**Fig. 6a**) captures the coincidence detection capabilities of CA1 pyramidal neurons, we constructed a pool of 10,000 CA1 pyramidal neurons (**Fig. 7a**). Every neuron received five streams of input drawn from two different Poisson distributions (EC vs. CA3). Each input stream was assigned to a single dendritic branch; two EC streams impinged onto the distal tuft segments, whereas three CA3 streams impinged onto the oblique dendrites and the distal trunk. To replicate the experiments of Jarsky et al[61] regarding the response of CA1 pyramidal neurons to EC, CA3, and EC + CA3 input, we adjusted the average rates (λ) of the Poisson distributions so that: a) When only the EC pathway is active, neurons have a moderate probability (>55%) of generating at least one distal dSpike, but no somatic APs (**Fig. S4a, Fig. S5a**). b) When only the CA3 pathway is active, neurons generate neither dendritic nor somatic spikes (**Fig. S4b, Fig. S5b**). c) The model outcome when simultaneously activating the two input pathways in the presence or absence of dendritic Na^+ VGICs is shown in (**Fig. 7b-c, Fig. S5b-c**).

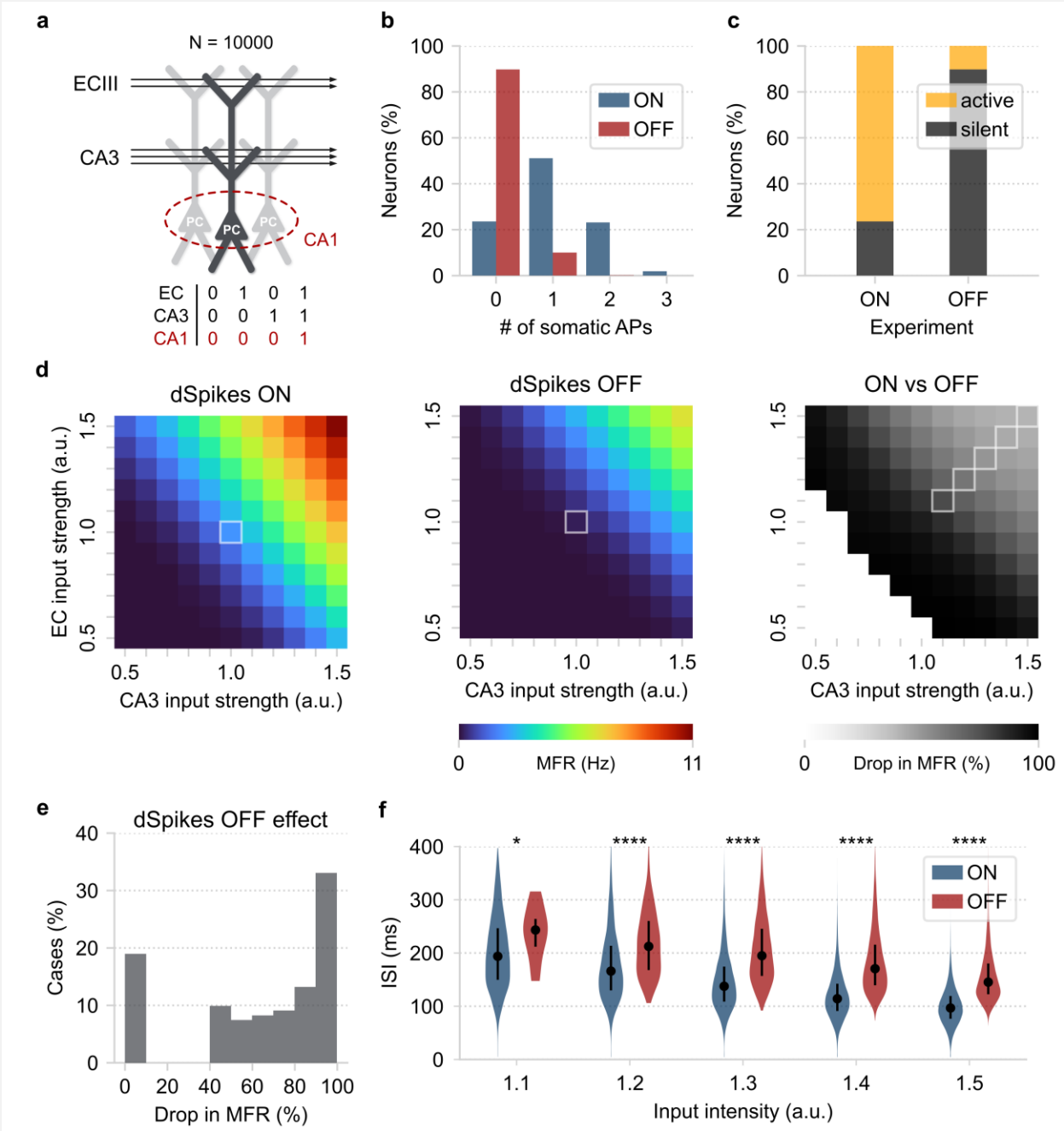

Figure 7 | Pathway interaction in a reduced CA1 network model. a) Schematic illustration of a pool of reduced compartmental CA1 PCs (N = 10,000). The arrows represent the two streams of input (independent Poisson-distributed spike trains) projecting to distinct dendritic segments. Each neuron represents a repetition of the same experiment with independent Poisson-distributed inputs of the same average frequency. Bottom: table describing the conditional activation of CA1 PCs requiring coincident EC and CA3 input. **b)** Probability distribution of somatic

spike count, with (ON) or without (OFF) dendritic spikes when both EC and CA3 input is applied to the network. **c)** Summary of the results shown in panel b. Active neurons: PCs that fired ≥1 somatic spike. Notice the reduction of the active population size when dendritic spiking is turned off. **d)** Repeating the coincidence detection experiment for a broad range of input intensities. Left: Mean neuronal firing rate (MFR) for each combination of EC/CA3 input amplitudes. Centre: same as in Left but with dSpikes turned off. The highlighted squares indicate the initial experimental conditions for the data shown in panels b and c. Right: quantifying the decrease in coincidence detection efficacy by measuring the MFR percentage decrease (dSpikes ON vs. dSpikes OFF). Deactivation of dendritic spiking results in reduced MFR in all cases tested. The white squares (bottom left) represent cases with very low initial MFR (< 0.1 Hz or < 5% network activity) that were excluded from the analysis. The highlighted squares indicate the experimental conditions of the data shown in panel f. **e)** Distribution of the results shown in panel d (right). **f)** Comparing the ISI distributions between the dSpikes ON and OFF conditions, using the highlighted cases in panel d (right). The circles represent the distribution medians and the vertical lines the first and third quantiles containing 50% of the data. Stars denote significance with unpaired t test (two-tailed) with Bonferroni's correction. The simulations and analysis code related to the above figure will be provided upon reasonable request, and will be freely available upon publication.

In control conditions (dSpikes ON), most neurons (~80 %) generated one or more somatic spikes when both the EC and CA3 pathways were active. The rest of the population remained silent throughout the 500 ms of the simulation duration. Deactivating dendritic spikes (dSpikes OFF) impacted neuronal firing significantly: the percentage of active neurons dropped to ~10%, signifying a ~70% decrease compared to the control experiment (dSpikes ON). In addition, all active neurons fired just a single somatic spike. This finding is in line with previous studies[61] and suggests a direct link between dendritic spiking and the conditional activation of CA1 PCs.

293 Importantly, it highlights our model's ability to reproduce complex pathway interaction rules
294 discovered in biological neurons beyond their basic dendritic properties (**Fig. 6**).

295 We next performed a parametric exploration of the input space to gain more insight into
296 the above phenomenon and assess its robustness (**Fig. 7d**). Specifically, we created ten input
297 distributions for each pathway, with firing rates that varied by 50-150% (with step 10%) of the
298 original values. This led to 121 EC / CA3 inputs combinations, which were then tested in the
299 presence and absence of dSpikes. Coincidence detection efficacy was estimated using the mean
300 neuronal firing rate (MFR) for every combination of inputs (**Fig. 7d left, center**). This metric
301 provides a quantitive way of gauging the dendritic effect on somatic output (**Fig. 7b**) rather than
302 simply recording the percentage of active neurons.

303 We found that dSpike deactivation greatly decreased the estimated MFR across all input
304 combinations (**Fig. 7d right**). This drop in MFR ranged between 40-100% (**Fig. 7e**); cases with
305 lower initial activity were prone to complete silencing, whereas high-activity cases were affected
306 to a lesser extent. Moreover, dendritic spiking significantly decreased the inter-spike intervals
307 (ISI) of somatic APs (**Fig. 7f**). The increased excitability caused by dSpikes resulted in somatic
308 responses with lower ISIs, close to those reported during bursting. However, in agreement with
309 experimental data[62,63], the simulated neurons did not generate actual somatic bursts since this
310 behavior requires the presence of dendritic Ca^{2+} plateau potentials, which are not included in our
311 model.

312 Overall, this example highlighted the ability of our simplified neuron models to reproduce
313 coincidence detection rules intrinsic to the dendrites of biological CA1 PCs. Moreover, we verified

314 the robustness of this behavior through a wide variety of EC/CA3 input parameters. Finally, we
315 showed that dendritic Na^+ spikes determine the frequency of somatic output in response to
316 coincident input and their temporal precision, reducing the threshold for strong somatic
317 activity[62].

318 Discussion

319 Establishing a rapport between biological and artificial neural networks is necessary for
320 understanding and hopefully replicating our brain's superior computing capabilities[2,3,64].
321 However, despite decades of research revealing the central role of dendrites in neuronal
322 information processing[1,4,5,34], the dendritic contributions to network-level functions remain
323 largely unexplored. *Dendrify* aims to promote the development of realistic spiking network
324 models by providing a theoretical framework and a modeling toolkit for efficiently adding
325 bioinspired dendritic mechanisms to SNNs. This is materialized by developing simplified yet
326 biologically accurate neuron models, optimal for network simulations in the *Brian 2* simulator[33].

327 Here, we demonstrated the ability of simple phenomenological models developed with
328 *Dendrify* to reproduce numerous experimentally observed dendritic functions. First, we showed
329 that even a generic toy model with passive dendrites can display some electrical segmentation
330 due to the resistance between its compartments (**Fig. 2**). This property allows dendrites to
331 operate semi-autonomously from the soma and multiple input integration sites to coexist within
332 a single neuron[35]. Next, we showed that adding dendritic Na^+ VGICs to a basic four-compartment
333 model (**Fig. 4**) unlocks important dendritic features that include: a) the presence of branch-
334 specific integration rules affected by local dendritic morphology[34], b) the supralinear summation

335 of correlated synaptic inputs and its impact on neuronal output[35], c) the generation of BPAPs as
336 feedback signals of neuronal activity[36,43,59]. Finally, we built a simplified yet biologically
337 constrained model of a CA1 PC (**Fig. 6**) and showed its ability to capture numerous passive (τ_m,
338 R_{input}, sag ratio, somatodendritic attenuation) and active (F-I curve, nonlinear dendritic
339 integration, BPAPs generation) properties of real CA1 PCs. Notably, the reduced model
340 reproduced complex coincidence detection rules found in CA1 PC dendrites and the impact of
341 Na^+ dSpikes on the frequency and the temporal precision of neuronal output[10,65] (**Fig. 7**). Overall,
342 we illustrated that *Dendrify* allows for building simple, mathematically tractable models that
343 replicate essential dendritic functions and their influence on neuronal activity.

344 Multiple recent SNNs studies seemingly converge to the same conclusion; neural
345 heterogeneity within a network can positively impact its learning and information processing
346 capabilities[3]. For example, heterogeneous SNNs with dynamic neuronal properties, such as
347 learnable adaptation[66] and membrane[67] time constants or a slowly moving firing threshold[68],
348 performed better in complex tasks like image classification or playing Atari games. Since
349 dendrites constitute a significant source of heterogeneity in biological networks, we expect that
350 transferring their properties into SNNs can confer important computational advantages. These
351 include a) the coexistence of numerous semi-independent integration sites within a single
352 neuron[34], b) flexible and adaptive information processing that adjusts to computational
353 demand[69], c) the presence of multi-timescale dynamics[37], and d) synergy between different
354 synaptic plasticity rules[20]. Indeed, few recent studies suggest that combining nonlinear dendritic
355 mechanisms with local learning rules provides SNNs with compelling advantages over previous
356 modeling standards. In particular, dendritic SNNs prolong memory retention in an associative

357 task[20] and enable sophisticated credit assignment in hierarchical circuits[59]. However, despite
358 noteworthy progress, we have a long way to go until we fully understand the implications of
359 dendritic processing in neural network functions.

360 *Dendrify* enables the development of reduced phenomenological neuron models that
361 preserve many essential properties of their biological counterparts. It is designed for non-experts
362 to increase its attractiveness to both experimental and theoretical groups interested in
363 developing bioinspired SNNs. Although software tools that help create reduced neuron models
364 are readily available[26,48], they rely on the HH formalism to simulate VGICs across the
365 somatodendritic axis. Here, by modeling dSpike mechanisms in an event-driven fashion, we
366 significantly reduce model complexity while maintaining high biological accuracy. Moreover,
367 contrary to similar known approaches[20], dSpikes and BPAPs are not simulated by clamping
368 segment voltages, allowing multiple synaptic or dendritic currents to be summed as in real
369 neurons. Notably, the proposed approach requires a relatively small number of free parameters,
370 resulting in straightforward model development and calibration. The latter is also facilitated by
371 the intuitiveness and the powerful features of the *Brian 2* simulator, which has seamless
372 compatibility with *Dendrify* and requires only basic knowledge of the *Python* programming
373 language. Finally, our approach allows testing new algorithms compatible with neuromorphic
374 hardware[70,71], which has seen impressive resource-saving benefits by including dendrites[72]. We
375 expect Dendrify to be a valuable tool for anyone interested in developing SNNs with a high degree
376 of bioinspiration to study how single-cell properties can influence network-level functions.

377 It is important to note that the presented modeling framework does not come without any
378 limitations. First, reduced compartmental models cannot compete with morphologically detailed

379 models in terms of spatial resolution. More specifically, in detailed models, each dendrite consists
380 of several segments used to ensure numerical simulation stability and allow more sophisticated
381 and realistic synaptic placement. In addition, since we do not utilize the HH formalism, certain
382 experimentally observed phenomena cannot be replicated by the standard models provided with
383 *Dendrify.* These include the depolarization block emerging in response to strong current
384 injections[73] or the reduction of backpropagation efficiency observed in some neuronal types
385 during prolonged somatic activity[59]. Moreover, the current version of *Dendrify* supports only Na^+
386 and partially Ca^{2+} VGICs and ignores many other known ion channel types[74]. Finally, synaptic
387 plasticity rules must be manually implemented using the standard *Brian 2* objects. However,
388 *Dendrify* is a project in continuous development, and based on the community feedback, many
389 new features or improvements will be included in future updates.

390 In summary, we introduced a novel theoretical framework and a set of tools to allow the
391 seamless development of reduced yet realistic spiking models of any neuronal type. We hope the
392 tool will be readily adopted by neuroscientists and neuromorphic engineers, facilitating
393 knowledge discovery while advancing the development of powerful brain-inspired artificial
394 computing systems.

395

396 # Methods

397 Code availability

398 *Dendrify's* code and detailed interactive *Python* notebooks related to all manuscript figures will
399 be freely available on *GitHub*.

400 Somatic compartment

401 The CA1 PC neuronal model is simulated as a leaky integrate-and-fire (I&F) model with
402 adaptation. The equations that govern the dynamics of the soma are

403 $$\mathrm{C}_{\mathrm{m}}^{s}\frac{\mathrm{d}V_{\mathrm{m}}^{s}}{\mathrm{d}t} = -\bar{\mathrm{g}}_{L}^{s}(V_{\mathrm{m}}^{s} - E_{L}^{s}) - \mathrm{g}_{A}(V_{\mathrm{m}}^{s} - E_{A}) + \sum_{i\in\mathcal{C}^{s}} I_{a}^{i,s} + \sum_{j\in\mathcal{S}^{s}} I_{\mathrm{syn}}^{j,s} + I_{\mathrm{ext}}^{s}$$

404 $$\tau_{A}\frac{\mathrm{d}\mathrm{g}_{A}}{\mathrm{d}t} = \bar{\mathrm{g}}_{A}|V_{\mathrm{m}}^{s} - V_{A}| - \mathrm{g}_{A}$$

405 where V_{m}^{s} denotes the somatic membrane voltage, $\mathrm{C}_{\mathrm{m}}^{s}$ the membrane capacitance, $\bar{\mathrm{g}}_{L}^{s}$ the
406 constant leak conductance, E_{L}^{s} the leak reversal potential, g_{A} the adaptation conductance, E_{A}
407 the adaptation reversal potential, $I_{a}^{i,s}$ the axial current from the i-th compartment connected to
408 the soma, $\mathcal{C}^{s}$ the set with all compartments that are connected with the soma, $I_{syn}^{j,s}$ a current
409 describing the effect of synaptic input from the j-th presynaptic neuron to the soma, $\mathcal{S}^{s}$ a set
410 with the presynaptic neurons connected to the soma, and I_{ext}^{s} denotes an external current
411 injected into the somatic compartment (similarly to an intracellular electrode). The adaptive
412 conductance is changing over time with τ_{A} denoting the time constant of the adaptation, and $\bar{\mathrm{g}}_{A}$
413 is the maximum conductance of the adaptation current. $|\cdot|$ denotes the absolute value.

414 When the somatic voltage crosses a threshold, V_{th}, a spike is generated. Here, we modified the
415 traditional approach of the I&F models, where after a spike generation, the voltage resets back
416 to a predetermined value, V_{reset}, and we include two resets, one that drives the voltage instantly
417 to a high value, V_{spike}, to account for the biological spike amplitude, and we incrementally
418 increase the g_{A} by a constant amount b, to account for the spike-triggered adaptation, and then

after a short decay, we instantly reset the voltage to V_{reset}. Mathematically, we describe this process as

$$if\ V_{\mathrm{m}}^{s} > V_{\mathrm{th}}\ then \begin{cases} V_{\mathrm{m}}^{s} \leftarrow V_{\mathrm{spike}} \\ \mathrm{g}_{A} \leftarrow \mathrm{g}_{A} + b \\ t_{\mathrm{spike}} \leftarrow t \end{cases}$$

$$if\ t = t_{\mathrm{spike}} + 0.5\mathrm{ms}\ \mathrm{then}\ V_{\mathrm{m}}^{s} \leftarrow V_{\mathrm{reset}}$$

<u>Dendritic compartments</u>

The dendritic compartments are governed by a similar equation for their dynamics, without the adaptation current and by adding two additional terms that control the simulation of the dendritic spikes.

$$\mathrm{C}_{\mathrm{m}}^{d}\frac{\mathrm{d}V_{\mathrm{m}}^{d}}{\mathrm{d}t} = -\bar{\mathrm{g}}_{L}^{d}\left(V_{\mathrm{m}}^{d} - E_{L}^{d}\right) + \sum_{i\in\mathcal{C}^{d}} I_{a}^{i,d} + \sum_{j\in\mathcal{S}^{d}} I_{\mathrm{syn}}^{j,d} + I_{\mathrm{Na}}^{d} + I_{\mathrm{K_{dr}}}^{d} + I_{\mathrm{ext}}^{d}$$

$$I_{\mathrm{Na}}^{d} = -\mathrm{g}_{\mathrm{Na}}^{d}(V_{\mathrm{m}}^{d} - E_{\mathrm{Na}})f_{\mathrm{Na}}$$

$$I_{\mathrm{K_{dr}}}^{d} = -\mathrm{g}_{\mathrm{K_{dr}}}^{d}(V_{\mathrm{m}}^{d} - E_{\mathrm{K}})f_{\mathrm{K_{dr}}}$$

$$\tau_{\mathrm{Na}}\frac{\mathrm{d}I_{\mathrm{Na}}^{d}}{\mathrm{d}t} = -I_{\mathrm{Na}}^{d}$$

$$\tau_{\mathrm{K_{dr}}}\frac{\mathrm{d}I_{\mathrm{K_{dr}}}^{d}}{\mathrm{d}t} = -I_{\mathrm{K_{dr}}}^{d}$$

where the I_{Na}^{d} and $I_{\mathrm{K_{dr}}}^{d}$ denote the sodium (Na^{+}) and the delayed-rectified potassium (K^{+}) currents, respectively. $\mathrm{g}_{\mathrm{Na}}^{d}$ and $\mathrm{g}_{\mathrm{K_{dr}}}^{d}$ are the corresponding conductances. These currents are

simulated as exponential decays, with time constants τ_{Na} and $\tau_{\mathrm{K_{dr}}}$, respectively. f_{Na} and $f_{\mathrm{K_{dr}}}$ are Boolean parameters indicating the generation of a dendritic spike.

<u>Dendritic spike mechanism</u>

To activate the sodium current, the V_{m}^{d} must cross a threshold, f_{Na} to be equal to 1, and to be outside of the refractory period of the sodium current:

$$if \begin{cases} V_{\mathrm{m}}^{d} > V_{th}^{d} \\ f_{\mathrm{Na}} = 1 \\ t > t_{\mathrm{spike}}^{d} + t_{ref}^{\mathrm{Na}} \end{cases} then \begin{cases} \mathrm{g}_{\mathrm{Na}}^{d} \leftarrow \mathrm{g}_{\mathrm{Na}}^{d} + \bar{\mathrm{g}}_{\mathrm{Na}}^{d} \\ f_{\mathrm{Na}} \leftarrow 0 \\ f_{\mathrm{K_{dr}}} \leftarrow 1 \\ t_{\mathrm{spike}}^{d} \leftarrow t \end{cases}$$

where t_{ref}^{Na} is the refractory period during which another dendritic spike cannot be generated, $\bar{\mathrm{g}}_{\mathrm{Na}}^{d}$ is the increase in conductance, and t_{spike}^{d} denotes the time that voltage crosses the threshold.

To activate the potassium current, a time delay should have passed and $f_{\mathrm{K_{dr}}}$ should be equal to 1.

$$if \begin{cases} t > t_{\mathrm{spike}}^{d} + t_{offset}^{\mathrm{K_{dr}}} \\ f_{\mathrm{K_{dr}}} = 1 \end{cases} then \begin{cases} \mathrm{g}_{\mathrm{K_{dr}}}^{d} \leftarrow \mathrm{g}_{\mathrm{K_{dr}}}^{d} + \bar{\mathrm{g}}_{\mathrm{K_{dr}}}^{d} \\ f_{\mathrm{Na}} \leftarrow 1 \\ f_{\mathrm{K_{dr}}} \leftarrow 0 \end{cases}$$

where $t_{offset}^{\mathrm{K_{dr}}}$ denotes the time-delay in potassium current generation, and $\bar{\mathrm{g}}_{\mathrm{K_{dr}}}^{d}$ is the increase in conductance.

In particular, when the dendritic membrane voltage crosses a threshold, a sodium current is applied, and after a delayed time, a potassium current is generated.

Axial currents between compartments

Each compartment receives an axial current as a sum over all axial current flowing towards it and coming from the connected compartments. The total axial current of the k-th compartment of the neuronal model is

$$I_a^k = \sum_{i \in \mathcal{C}^k} I_a^{i,k}$$

where $\mathcal{C}^k$ denotes all compartments that are connected with the k-th compartment. Each compartment-specific axial current is given by

$$I_a^{i,k} = \mathrm{g}_c^{i,k}\left(V_\mathrm{m}^k - V_\mathrm{m}^i\right)$$

where the $\mathrm{g}_c^{i,k}$ denotes the coupling conductance between the i-th and k-th compartments.

We use two approaches to calculate the $\mathrm{g}_c^{i,k}$ based on the morphological properties of the compartments.

When the total number of compartments is low and the adjacent-to-soma compartments are highly coupled with the soma, we calculate the coupling conductance as the reverse R_long

$$R_\mathrm{long} = \frac{r_a l^k}{\pi\left(\frac{d^k}{2}\right)^2} \Rightarrow \mathrm{g}_c^{i,k} = \frac{1}{R_\mathrm{long}}$$

where d^k denotes the diameter of the k-th compartment, l^k its length and r_a its specific axial resistance in $\Omega \cdot \mathrm{cm}$. The coupling conductance is given in S (siemens). Thus, the axial current is calculated in absolute units, i.e., A (ampere).

The second method uses the half-cylinder approach, where the coupling term of two adjacent compartments is calculated between their centers.

$$R_{\text{long}} = \frac{1}{2}\left(\frac{r_a l^k}{\pi\left(\frac{d^k}{2}\right)^2} + \frac{r_a l^i}{\pi\left(\frac{d^i}{2}\right)^2}\right) \Rightarrow \mathrm{g}_c^{i,k} = \frac{1}{R_{\text{long}}}$$

Notice that we did not divide by the surface area of interest as we wrote the differential equations in absolute terms. Thus, two adjacent compartments have the same coupling conductance $\mathrm{g}_c^{i,k} = \mathrm{g}_c^{k,i}$.

<u>Global and specific properties</u>

We assume that all compartments are cylinders with known diameter d and length l. The surface area of the i-th compartment (open cylinder) is given by:

$$A^i = 2\pi\left(\frac{d^i}{2}\right) l^i$$

and its total membrane capacitance and leak conductance are given by:

$$\mathrm{C}_{\mathrm{m}}^i = c_{\mathrm{m}}^i A^i, \bar{\mathrm{g}}_L^i = \frac{1}{r_{\mathrm{m}}^i} A^i$$

where c_{m}^i is the specific capacitance in $\mathrm{uF/cm^2}$ and r_{m}^i is the specific membrane resistivity in $\Omega \cdot \mathrm{cm}^2$.

<u>Synaptic currents</u>

The synaptic currents that can flow to each compartment can be AMPA, NMDA, or GABA. The mathematical description is:

$$I_{\mathrm{syn}}^{i}(t) = \bar{\mathrm{g}}_{\mathrm{syn}}^{i} f_{\mathrm{syn}}\left(\tau_{\mathrm{syn}}^{\mathrm{rise}}, \tau_{\mathrm{syn}}^{\mathrm{decay}}\right) s_{\mathrm{syn}}^{i}(t)\left(V_{\mathrm{m}}^{i} - E_{\mathrm{syn}}\right)\sigma\left(V_{\mathrm{m}}^{i}\right), \mathrm{syn} \in \{\mathrm{AMPA}, \mathrm{NMDA}, \mathrm{GABA}\}$$

where $f_{\mathrm{syn}}\left(\tau_{\mathrm{syn}}^{\mathrm{rise}}, \tau_{\mathrm{syn}}^{\mathrm{decay}}\right)$ is a normalization factor dependent on the rise and decay time constants ($\tau_{\mathrm{syn}}^{\mathrm{rise}}$ and $\tau_{\mathrm{syn}}^{\mathrm{decay}}$) to ensure that for every presynaptic spike, the maximum conductance is $\bar{\mathrm{g}}_{\mathrm{syn}}^{i}$, i.e., the $f_{\mathrm{syn}}\left(\tau_{\mathrm{syn}}^{\mathrm{rise}}, \tau_{\mathrm{syn}}^{\mathrm{decay}}\right)\mathrm{s}_{\mathrm{syn}}^{i}(t)$ term is bounded in [0,1].

The $s_{\mathrm{syn}}^{i}(t)$ term denotes the time-dependence of the synaptic conductance. Here, we use two methods; one with a dual exponential form as we want to set the rise and decay times independently, and the other as a simple exponential decay.

The dual exponential function is given by:

$$s_{\mathrm{syn}}^{i}(t) = H\left(t - t_{pre}\right)\left(\exp\left(-\frac{t - t_{pre}}{\tau_{\mathrm{syn}}^{\mathrm{decay}}}\right) - \exp\left(-\frac{t - t_{pre}}{\tau_{\mathrm{syn}}^{\mathrm{rise}}}\right)\right)$$

where $H(z)$ denotes the Heaviside function

$$H(z) = \begin{cases} 1, \text{if } z \geq 0 \\ 0, \text{if } z < 0 \end{cases}$$

The normalization factor is the peak value of s_{syn}^{i} at time t_{peak}.

$$\frac{\mathrm{d}s_{\mathrm{syn}}^{i}}{\mathrm{d}t} \overset{\mathrm{set}}{=} 0 \Leftrightarrow t_{peak} = \frac{\tau_{\mathrm{syn}}^{\mathrm{decay}}\tau_{\mathrm{syn}}^{\mathrm{rise}}}{\tau_{\mathrm{syn}}^{\mathrm{decay}} - \tau_{\mathrm{syn}}^{\mathrm{rise}}} \ln\left(\frac{\tau_{\mathrm{syn}}^{\mathrm{decay}}}{\tau_{\mathrm{syn}}^{\mathrm{rise}}}\right) + t_{pre}$$

$$f_{\mathrm{syn}}\left(\tau_{\mathrm{syn}}^{\mathrm{rise}}, \tau_{\mathrm{syn}}^{\mathrm{decay}}\right) = \frac{1}{s_{\mathrm{syn}}^{i}\left(t_{peak}\right)}$$

For AMPA and GABA currents, the voltage-dependence is neglected, i.e., $\sigma\left(V_{\mathrm{m}}^{i}\right) = 1$. For the NMDA currents, which are voltage-dependent due to magnesium (Mg^{2+}) blockade, the sigmoidal function σ is given:

$$\sigma\left(V_{\mathrm{m}}^{i}\right) = \frac{1}{1 + \frac{[\mathrm{Mg}^{2+}]_{\mathrm{o}}}{\beta} \cdot \exp\left(-\alpha\left(V_{\mathrm{m}}^{i} - \gamma\right)\right)}$$

where β (mM), α (mV^{-1}) and γ (mV) control the magnesium and voltage dependencies, respectively, and $[\mathrm{Mg}^{2+}]_{\mathrm{o}}$ denotes the external magnesium concentration, usually set at a predetermined and constant level (in mM).

The dynamics of the synaptic conductance are given by a set of two differential equations that simulate the double exponential relationship found in synapses:

$$\frac{\mathrm{d}s_{\mathrm{syn}}^{i}}{\mathrm{d}t} = -\frac{s_{\mathrm{syn}}^{i}}{\tau_{\mathrm{syn}}^{\mathrm{decay}}} + \frac{x_{\mathrm{syn}}^{i}\left(1 - s_{\mathrm{syn}}^{i}\right)}{\tau_{\mathrm{syn}}^{\mathrm{rise}}}$$

$$\frac{\mathrm{d}x_{\mathrm{syn}}^{i}}{\mathrm{d}t} = -\frac{x_{\mathrm{syn}}^{i}}{\tau_{\mathrm{syn}}^{\mathrm{rise}}}$$

$$if\ t = t_{pre}\ then\ x_{\mathrm{syn}}^{i} \leftarrow x_{\mathrm{syn}}^{i} + 1$$

The simple decay function is given by:

$$s_{\mathrm{syn}}^{i}(t) = H\left(t - t_{pre}\right) \exp\left(-\frac{t - t_{pre}}{\tau_{\mathrm{syn}}^{\mathrm{decay}}}\right)$$

The dynamics of the synaptic conductance is governed by one differential equation:

$$\frac{\mathrm{d}s_{\mathrm{syn}}^{i}}{\mathrm{d}t} = -\frac{s_{\mathrm{syn}}^{i}}{\tau_{\mathrm{syn}}^{\mathrm{decay}}}$$

$$if\ t = t_{pre}\ then\ s_{\mathrm{syn}}^{i} \leftarrow s_{\mathrm{syn}}^{i} + 1.$$

The normalization function when the simple decay method is applied is $f_{\mathrm{syn}} = 1$.

As a compartment can receive more than one presynaptic connection of the same type and/or synapses of different type simultaneously, the total synaptic current of the i-th compartment is given by:

$$\begin{aligned} I_{\mathrm{syn}}^{i}(t) = {} & \bar{\mathrm{g}}_{\mathrm{AMPA}}^{i}\left(V_{\mathrm{m}}^{i} - E_{\mathrm{AMPA}}\right) f_{\mathrm{AMPA}} \sum_{j \in \mathcal{S}_{\mathrm{AMPA}}^{i}} s_{\mathrm{AMPA}}^{j,i}(t) \\ & + \bar{\mathrm{g}}_{\mathrm{NMDA}}^{i}\left(V_{\mathrm{m}}^{i} - E_{\mathrm{NMDA}}\right) f_{\mathrm{NMDA}} \sum_{j \in \mathcal{S}_{\mathrm{NMDA}}^{i}} s_{\mathrm{NMDA}}^{j,i}(t) \\ & + \bar{\mathrm{g}}_{\mathrm{GABA}}^{i}\left(V_{\mathrm{m}}^{i} - E_{\mathrm{GABA}}\right) \sigma\left(V_{\mathrm{m}}^{i}\right) f_{\mathrm{GABA}} \sum_{j \in \mathcal{S}_{\mathrm{GABA}}^{i}} s_{\mathrm{GABA}}^{j,i}(t). \end{aligned}$$

<u>A practical guide for developing reduced models with bioinspired properties.</u>

Here, we provide a step-by-step guide for developing simplified compartmental models that capture key electrophysiological and anatomical features of their biological counterparts. The proposed protocol relies on the previous work of Bush & Sejnowski[21] and focuses on achieving realistic axial resistance ($\boldsymbol{r_a}$), input resistance ($\boldsymbol{R_{in}}$) and membrane time constant ($\boldsymbol{\tau_{\mathrm{m}}}$) along with accurate positioning of synaptic inputs and ionic conductances. We illustrate this approach by

528 breaking down the development and validation of a reduced CA1 pyramidal cell (CA1 PC).

529 **Step 1: Identify the most important anatomical and functional regions found in the neuronal**

530 **morphology**

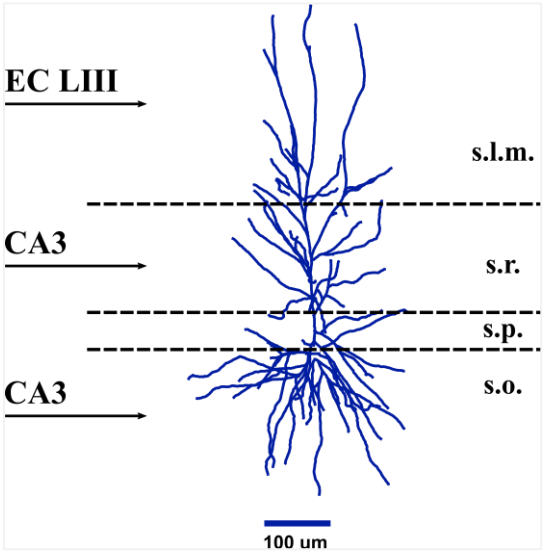

Reconstruction of a human CA1 PC
(adopted from the neuromorpho.org)

531 Based on the CA1 region layering and the spatial segregation of external input pathways, CA1

532 pyramidal neurons can be partitioned into five functionally distinct neuronal regions[75]:

533 i. The perisomatic area → primary spiking unit (s. Pyramidale)

534 ii. The basal dendritic area → CA3 input receiver (s. Oriens)

535 iii. The proximal apical dendritic area → dendritic region devoid of spines (s. Radiatum, < 100

536 um from soma)

537 iv. The medial apical dendritic area → CA3 input receiver (s. Radiatum, > 100 um from soma)

538 v. The distal apical dendritic area → EC layer III input receiver (s. Lacunosum Moleculare)

539 **Step 2: Design a toy model capturing the main neuronal features identified in the previous step**

540 • Using cylindrical compartments, design a toy model that captures the main morphological
541 features of the neuron of interest. The number of model compartments should not be
542 less than the number of the identified, functionally unique neuronal regions. This would
543 prevent the model from processing the various input pathways semi-independently, as
544 occurs in real CA1 PCs[61].

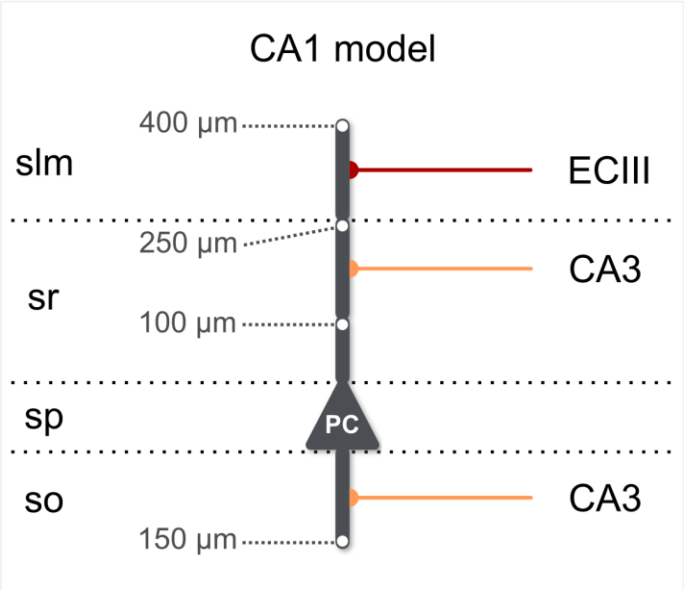

A basic five-compartment CA1 PC model

545 • If biological accuracy is more important than simulation performance, the number of
546 compartments can be further increased to account for more neuronal features. For
547 example, adding 4 compartments to the previous model allows to account for the

548 increased dendritic branching that is observed in the distal, medial and basal areas of CA1
549 PC dendrites. Other examples of morphologically reduced CA1 models can be seen in
550 Tomko et. al[47].

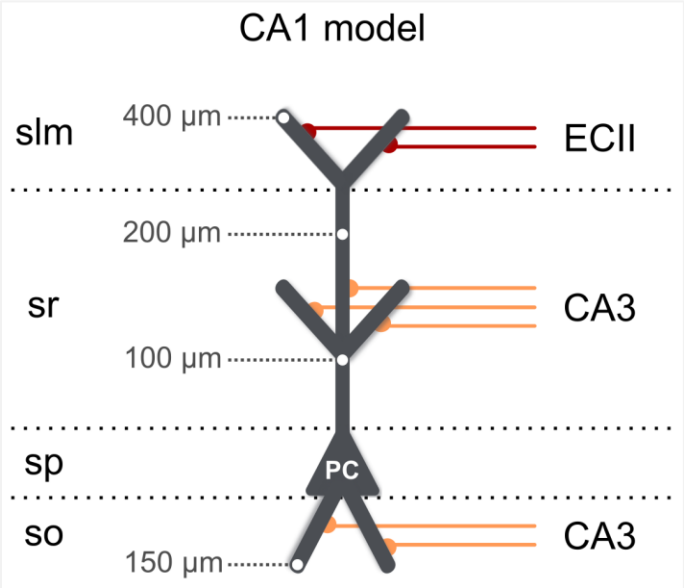

A nine-compartment CA1 PC model with a high degree of bioinspiration

551 Set the dimensions of the compartments according to the rules described by Bush & Sejnowski[21].
552 In short, their approach aims to preserve realistic attenuation of the currents traveling along the
553 somatodendritic axis. This is achieved by creating compartments that have correct electrotonic
554 length and a diameter that is representative of the dendritic diameter observed in real neurons.

555 If there is no detailed morphological data, you can set the cylinder lengths that approximate the
556 distance from soma and capture the decrease in dendritic diameter as you move away from the
557 soma. Due to immense biological variability, the solutions to this problem are infinite, and a single
558 most representative model is impossible to exist.

Step 3: Validation of passive parameters

<u>1) Membrane time constant</u>

- Start with the values of somatic capacitance (**C_m**) and leakage conductance (**g_L**). Set $\mathrm{C_m}$ equal to $1\ \mu\mathrm{F/cm^2}$ and choose the appropriate $\mathrm{g_L}$ value so that the desired membrane time constant (**τ_m**) is achieved according to the formula $\tau_\mathrm{m} = \mathrm{C_m}/\mathrm{g_L}$.
- Next, use the same values for the dendrites, but we multiply both by a factor of 1.2-2.0 (depends on experimental data, use 1.5 if this value is unknown) to account for the added area due to synaptic spines that are not explicitly modeled.

<u>2) Input resistance and somatodendritic attenuation</u>

- Set the axial resistance (**R_a**) according to experimental evidence, if available. Typical values range between 100-250 MOhm·cm.
- Test the attenuation of currents along the somatodendritic axis by applying long somatic current injections (Fig. 4). By default, *Dendrify* calculates the coupling conductances according to the half-cylinders formula[76]:

$$R_\mathrm{long} = \frac{1}{2}\left(\frac{r_a l^k}{\pi\left(\frac{d^k}{2}\right)^2} + \frac{r_a l^i}{\pi\left(\frac{d^i}{2}\right)^2}\right) \Rightarrow \mathrm{g}_c^{i,k} = \frac{1}{R_\mathrm{long}}$$

where scripts i and k denote two adjacent compartments, and l, d denote the length and the diameter of the compartments, respectively.

577 Importantly, small manual corrections might be necessary to achieve more realistic attenuation.

578 • Calculate the 'model's input resistance (R_{in}) by using a typical, hyperpolarizing current
579 step protocol[45]. Most likely, the initial values will deviate from the experimental values
580 due to the reduced membrane area of the simplified model. This is why we multiply both
581 $\mathrm{C_m}$ and $\mathrm{g_L}$ (somatic and dendritic) with the same scale factor until the model reaches the
582 desired R_{in} as explained here[21].

583 **Step 4: Validation of active properties**

584 This step assumes that for the soma, an I&F model with adaptation is used such as the AdEx[77],
585 CAdEx[78] or Izhikevich[79] model. Use somatic current injections to validate the Rheobase and FI
586 curve by adjusting the model variables based on the model-specific guidelines.

587 **Step 5: Validation of dendritic integration**

588 The last step includes the validation of the Na^+ dendritic spike. First, we set a realistic $\mathrm{g_{Na}}$ to $\mathrm{g_K}$
589 ratio, based on experimental evidence. Then, we set a voltage threshold, which denotes the
590 membrane voltage values above which a dSpike is initiated. To account for the geometrical
591 characteristics of the dendritic compartments, we multiply both conductances with the
592 compartmental surface area, i.e., A^i. Using the validation protocol depicted in Fig. S3, we scale
593 the conductances to capture a realistic dSpike amplitude.

References

1. Poirazi, P. & Papoutsi, A. Illuminating dendritic function with computational models. *Nature Reviews Neuroscience* (2020) doi:10.1038/s41583-020-0301-7.

2. Christensen, D. V. *et al.* 2022 Roadmap on Neuromorphic Computing and Engineering. (2021).

3. Zenke, F. *et al.* Visualizing a joint future of neuroscience and neuromorphic engineering. in *Neuron* (2021). doi:10.1016/j.neuron.2021.01.009.

4. London, M. & Häusser, M. Dendritic computation. *Annual Review of Neuroscience* (2005) doi:10.1146/annurev.neuro.28.061604.135703.

5. Stuart, G. J. & Spruston, N. Dendritic integration: 60 years of progress. *Nature Neuroscience* (2015) doi:10.1038/nn.4157.

6. Kastellakis, G., Silva, A. J. & Poirazi, P. Linking Memories across Time via Neuronal and Dendritic Overlaps in Model Neurons with Active Dendrites. *Cell Rep.* (2016) doi:10.1016/j.celrep.2016.10.015.

7. Tzilivaki, A., Kastellakis, G. & Poirazi, P. Challenging the point neuron dogma: FS basket cells as 2-stage nonlinear integrators. *Nat. Commun.* (2019) doi:10.1038/s41467-019-11537-7.

611 8. Kaifosh, P. & Losonczy, A. Mnemonic Functions for Nonlinear Dendritic Integration in
612 Hippocampal Pyramidal Circuits. *Neuron* **90**, 622–634 (2016).

613 9. Bilash, O. M., Chavlis, S., Poirazi, P. & Basu, J. Lateral entorhinal cortex inputs modulate
614 hippocampal dendritic excitability by recruiting a local disinhibitory microcircuit. *bioRxiv*
615 2022.01.13.476247 (2022) doi:10.1101/2022.01.13.476247.

616 10. Ariav, G., Polsky, A. & Schiller, J. Submillisecond precision of the input-output
617 transformation function mediated by fast sodium dendritic spikes in basal dendrites of
618 CA1 pyramidal neurons. *J. Neurosci.* (2003) doi:10.1523/jneurosci.23-21-07750.2003.

619 11. Branco, T. & Häusser, M. Synaptic Integration Gradients in Single Cortical Pyramidal Cell
620 Dendrites. *Neuron* (2011) doi:10.1016/j.neuron.2011.02.006.

621 12. Polsky, A., Mel, B. W. & Schiller, J. Computational subunits in thin dendrites of pyramidal
622 cells. *Nat. Neurosci.* (2004) doi:10.1038/nn1253.

623 13. Softky, W. Sub-millisecond coincidence detection in active dendritic trees. *Neuroscience*
624 (1994) doi:10.1016/0306-4522(94)90154-6.

625 14. Ujfalussy, B. B., Makara, J. K., Lengyel, M. & Branco, T. Global and Multiplexed Dendritic
626 Computations under In Vivo-like Conditions. *Neuron* (2018)
627 doi:10.1016/j.neuron.2018.08.032.

628 15. Ujfalussy, B., Kiss, T. & Érdi, P. Parallel computational subunits in dentate granule cells
629 generate multiple place fields. *PLoS Comput. Biol.* (2009)
630 doi:10.1371/journal.pcbi.1000500.

631 16. Mel, B. W. & Schiller, J. On the fight between excitation and inhibition: location is
632 everything. *Science's STKE : signal transduction knowledge environment* (2004)
633 doi:10.1126/stke.2502004pe44.

634 17. Gidon, A. & Segev, I. Principles Governing the Operation of Synaptic Inhibition in
635 Dendrites. *Neuron* (2012) doi:10.1016/j.neuron.2012.05.015.

636 18. Kleindienst, T., Winnubst, J., Roth-Alpermann, C., Bonhoeffer, T. & Lohmann, C. Activity-
637 dependent clustering of functional synaptic inputs on developing hippocampal dendrites.
638 *Neuron* **72**, 1012–1024 (2011).

639 19. Kastellakis, G., Cai, D. J., Mednick, S. C., Silva, A. J. & Poirazi, P. Synaptic clustering within
640 dendrites: An emerging theory of memory formation. *Progress in Neurobiology* (2015)
641 doi:10.1016/j.pneurobio.2014.12.002.

642 20. Bono, J. & Clopath, C. Modeling somatic and dendritic spike mediated plasticity at the
643 single neuron and network level. *Nat. Commun.* **8**, (2017).

644 21. Bush, P. C. & Sejnowski, T. J. Reduced compartmental models of neocortical pyramidal
645 cells. *J. Neurosci. Methods* (1993) doi:10.1016/0165-0270(93)90151-G.

646 22. Destexhe, A. Simplified models of neocortical pyramidal cells preserving somatodendritic
647 voltage attenuation. *Neurocomputing* **38**–**40**, (2001).

648 23. Hendrickson, E. B., Edgerton, J. R. & Jaeger, D. The capabilities and limitations of
649 conductance-based compartmental neuron models with reduced branched or
650 unbranched morphologies and active dendrites. *J. Comput. Neurosci.* (2011)

651 doi:10.1007/s10827-010-0258-z.

652 24. Marasco, A., Limongiello, A. & Migliore, M. Fast and accurate low-dimensional reduction
653 of biophysically detailed neuron models. *Sci. Rep.* (2012) doi:10.1038/srep00928.

654 25. Lee, K. J. *et al.* Mossy Fiber-CA3 Synapses Mediate Homeostatic Plasticity in Mature
655 Hippocampal Neurons. *Neuron* **77**, 99–114 (2013).

656 26. Wybo, W. A. M. *et al.* Data-driven reduction of dendritic morphologies with preserved
657 dendro-somatic responses. *Elife* (2021) doi:10.7554/eLife.60936.

658 27. Chavlis, S., Petrantonakis, P. C. & Poirazi, P. Dendrites of Dentate Gyrus Granule Cells
659 Contribute to Pattern Separation by Controlling Sparsity. **110**, 89–110 (2017).

660 28. Papoutsi, A., Sidiropoulou, K. & Poirazi, P. Dendritic Nonlinearities Reduce Network Size
661 Requirements and Mediate ON and OFF States of Persistent Activity in a PFC Microcircuit
662 Model. *PLoS Comput. Biol.* (2014) doi:10.1371/journal.pcbi.1003764.

663 29. Wu, X., Liu, X., Li, W. & Wu, Q. Improved expressivity through dendritic neural networks.
664 in *Advances in Neural Information Processing Systems* (2018).

665 30. Chavlis, S. & Poirazi, P. Drawing inspiration from biological dendrites to empower
666 artificial neural networks. *Current Opinion in Neurobiology* (2021)
667 doi:10.1016/j.conb.2021.04.007.

668 31. Pinitas, K., Chavlis, S. & Poirazi, P. Dendritic Self-Organizing Maps for Continual Learning.
669 (2021) doi:10.48550/arxiv.2110.13611.

670 32. Grewal, K., Forest, J., Cohen, B. P. & Ahmad, S. Going Beyond the Point Neuron: Active

Dendrites and Sparse Representations for Continual Learning. *bioRxiv* 2021.10.25.465651 (2021) doi:10.1101/2021.10.25.465651.

33. Stimberg, M., Brette, R. & Goodman, D. F. M. Brian 2, an intuitive and efficient neural simulator. *Elife* (2019) doi:10.7554/eLife.47314.

34. Tran-Van-Minh, A. *et al.* Contribution of sublinear and supralinear dendritic integration to neuronal computations. *Front. Cell. Neurosci.* (2015) doi:10.3389/fncel.2015.00067.

35. Poirazi, P., Brannon, T. & Mel, B. W. Arithmetic of subthreshold synaptic summation in a model CA1 pyramidal cell. *Neuron* (2003) doi:10.1016/S0896-6273(03)00148-X.

36. Hausser, M., Spruston, N. & Stuart, G. J. Diversity and dynamics of dendritic signaling. *Science* (2000) doi:10.1126/science.290.5492.739.

37. Spruston, N. Pyramidal neurons: Dendritic structure and synaptic integration. *Nature Reviews Neuroscience* (2008) doi:10.1038/nrn2286.

38. Nevian, T., Larkum, M. E., Polsky, A. & Schiller, J. Properties of basal dendrites of layer 5 pyramidal neurons: A direct patch-clamp recording study. *Nat. Neurosci.* (2007) doi:10.1038/nn1826.

39. Losonczy, A. & Magee, J. C. Integrative Properties of Radial Oblique Dendrites in Hippocampal CA1 Pyramidal Neurons. *Neuron* (2006) doi:10.1016/j.neuron.2006.03.016.

40. Chiovini, B. *et al.* Dendritic Spikes Induce Ripples in Parvalbumin Interneurons during Hippocampal Sharp Waves. *Neuron* (2014) doi:10.1016/j.neuron.2014.04.004.

41. Colbert, C. M. Back-propagating action potentials in pyramidal neurons: A putative

691 signaling mechanism for the induction of Hebbian synaptic plasticity. *Restor. Neurol.*
692 *Neurosci.* (2002).

693 42. Sjöström, P. J. & Häusser, M. A Cooperative Switch Determines the Sign of Synaptic
694 Plasticity in Distal Dendrites of Neocortical Pyramidal Neurons. *Neuron* (2006)
695 doi:10.1016/j.neuron.2006.06.017.

696 43. Waters, J., Schaefer, A. & Sakmann, B. Backpropagating action potentials in neurones:
697 Measurement, mechanisms and potential functions. *Progress in Biophysics and*
698 *Molecular Biology* (2005) doi:10.1016/j.pbiomolbio.2004.06.009.

699 44. Kim, Y., Hsu, C. L., Cembrowski, M. S., Mensh, B. D. & Spruston, N. Dendritic sodium
700 spikes are required for long-term potentiation at distal synapses on hippocampal
701 pyramidal neurons. *Elife* (2015) doi:10.7554/eLife.06414.

702 45. Masurkar, A. V. *et al.* Postsynaptic integrative properties of dorsal CA1 pyramidal neuron
703 subpopulations. *J. Neurophysiol.* (2020) doi:10.1152/JN.00397.2019.

704 46. Golding, N. L., Mickus, T. J., Katz, Y., Kath, W. L. & Spruston, N. Factors mediating
705 powerful voltage attenuation along CA1 pyramidal neuron dendrites. *J. Physiol.* (2005)
706 doi:10.1113/jphysiol.2005.086793.

707 47. Tomko, M., Benuskova, L. & Jedlicka, P. A new reduced-morphology model for CA1
708 pyramidal cells and its validation and comparison with other models using HippoUnit. *Sci.*
709 *Rep.* (2021) doi:10.1038/s41598-021-87002-7.

710 48. Amsalem, O. *et al.* An efficient analytical reduction of detailed nonlinear neuron models.

711 *Nat. Commun.* (2020) doi:10.1038/s41467-019-13932-6.

712 49. Van Geit, W. *et al.* BluePyOpt: Leveraging open source software and cloud infrastructure
713 to optimise model parameters in neuroscience. *Front. Neuroinform.* (2016)
714 doi:10.3389/fninf.2016.00017.

715 50. Andersen, P., Morris, R., Amaral, D., Bliss, T. & O' Keefe, J. *The Hippocampus Book*. *The*
716 *Hippocampus Book* (2009). doi:10.1093/acprof:oso/9780195100273.001.0001.

717 51. Benavides-Piccione, R. *et al.* Differential Structure of Hippocampal CA1 Pyramidal
718 Neurons in the Human and Mouse. *Cereb. Cortex* (2020) doi:10.1093/cercor/bhz122.

719 52. Magee, J. C. & Cook, E. P. Somatic EPSP amplitude is independent of synapse location in
720 hippocampal pyramidal neurons. *Nat. Neurosci.* **3**, 895–903 (2000).

721 53. Andrásfalvy, B. K. & Magee, J. C. Distance-dependent increase in AMPA receptor number
722 in the dendrites of adult hippocampal CA1 pyramidal neurons. *J. Neurosci.* (2001)
723 doi:10.1523/jneurosci.21-23-09151.2001.

724 54. Otmakhova, N. A., Otmakhov, N. & Lisman, J. E. Pathway-specific properties of AMPA and
725 NMDA-mediated transmission in CA1 hippocampal pyramidal cells. *J. Neurosci.* (2002)
726 doi:10.1523/jneurosci.22-04-01199.2002.

727 55. Enoki, R. *et al.* NMDA receptor-mediated depolarizing after-potentials in the basal
728 dendrites of CA1 pyramidal neurons. *Neurosci. Res.* (2004)
729 doi:10.1016/j.neures.2003.11.011.

730 56. Bittner, K. C., Andrasfalvy, B. K. & Magee, J. C. Ion Channel Gradients in the Apical Tuft

731 Region of CA1 Pyramidal Neurons. *PLoS One* (2012) doi:10.1371/journal.pone.0046652.

732 57. Shipman, S. L., Herring, B. E., Suh, Y. H., Roche, K. W. & Nicoll, R. A. Distance-dependent
733 scaling of AMPARs is cell-autonomous and GluA2 dependent. *J. Neurosci.* (2013)
734 doi:10.1523/JNEUROSCI.0678-13.2013.

735 58. Migliore, R. *et al.* The physiological variability of channel density in hippocampal CA1
736 pyramidal cells and interneurons explored using a unified data-driven modeling
737 workflow. *PLoS Comput. Biol.* (2018) doi:10.1371/journal.pcbi.1006423.

738 59. Golding, N. L., Kath, W. L. & Spruston, N. Dichotomy of action-potential backpropagation
739 in CA1 pyramidal neuron dendrites. *J. Neurophysiol.* (2001)
740 doi:10.1152/jn.2001.86.6.2998.

741 60. Magee, J. C. & Cook, E. P. Somatic EPSP amplitude is independent of synapse location in
742 hippocampal pyramidal neurons. *Nat. Neurosci.* (2000) doi:10.1038/78800.

743 61. Jarsky, T., Roxin, A., Kath, W. L. & Spruston, N. Conditional dendritic spike propagation
744 following distal synaptic activation of hippocampal CA1 pyramidal neurons. *Nat.*
745 *Neurosci.* (2005) doi:10.1038/nn1599.

746 62. Takahashi, H. & Magee, J. C. Pathway Interactions and Synaptic Plasticity in the Dendritic
747 Tuft Regions of CA1 Pyramidal Neurons. *Neuron* (2009)
748 doi:10.1016/j.neuron.2009.03.007.

749 63. Bittner, K. C. *et al.* Conjunctive input processing drives feature selectivity in hippocampal
750 CA1 neurons. *Nat. Neurosci.* (2015) doi:10.1038/nn.4062.

64. Richards, B. A. *et al.* A deep learning framework for neuroscience. *Nature Neuroscience* (2019) doi:10.1038/s41593-019-0520-2.

65. Golding, N. L. & Spruston, N. Dendritic sodium spikes are variable triggers of axonal action potentials in hippocampal CA1 pyramidal neurons. *Neuron* (1998) doi:10.1016/S0896-6273(00)80635-2.

66. Yin, B., Corradi, F. & Bohté, S. M. Effective and Efficient Computation with Multiple-timescale Spiking Recurrent Neural Networks. in *ACM International Conference Proceeding Series* (2020). doi:10.1145/3407197.3407225.

67. Perez-Nieves, N., Leung, V. C. H., Dragotti, P. L. & Goodman, D. F. M. Neural heterogeneity promotes robust learning. *Nat. Commun.* (2021) doi:10.1038/s41467-021-26022-3.

68. Bellec, G. *et al.* A solution to the learning dilemma for recurrent networks of spiking neurons. *Nat. Commun.* (2020) doi:10.1038/s41467-020-17236-y.

69. Poleg-Polsky, A. Dendritic spikes expand the range of well tolerated population noise structures. *J. Neurosci.* (2019) doi:10.1523/JNEUROSCI.0638-19.2019.

70. Indiveri, G. *et al.* Neuromorphic silicon neuron circuits. *Frontiers in Neuroscience* (2011) doi:10.3389/fnins.2011.00073.

71. Michaelis, C., Lehr, A. B., Oed, W. & Tetzlaff, C. Brian2Loihi: An emulator for the neuromorphic chip Loihi using the spiking neural network simulator Brian. (2021).

72. Li, X. *et al.* Power-efficient neural network with artificial dendrites. *Nat. Nanotechnol.*

(2020) doi:10.1038/s41565-020-0722-5.

73. Bianchi, D. *et al.* On the mechanisms underlying the depolarization block in the spiking dynamics of CA1 pyramidal neurons. *J. Comput. Neurosci.* (2012) doi:10.1007/s10827-012-0383-y.

74. Stuart, G., Spruston, N. & Häusser, M. *Dendrites*. *Dendrites* (2012). doi:10.1093/acprof:oso/9780198566564.001.0001.

75. Andersen, P., Morris, R., Amaral, D., Bliss, T. & O' Keefe, J. *The Hippocampus Book*. *The Hippocampus Book* (2009). doi:10.1093/acprof:oso/9780195100273.001.0001.

76. Ermentrout, G. B. & Terman, D. H. Mathematical foundations of neuroscience. in *Interdisciplinary Applied Mathematics* (2010).

77. Romain Brette, W. G. Adaptive Exponential Integrate-and-Fire Model as an Effective Description of Neuronal Activity. *J. Neurophysiol.* (2005) doi:10.1152/jn.00686.2005.

78. Górski, T., Depannemaecker, D. & Destexhe, A. Conductance-based adaptive exponential integrate-and-fire model. *Neural Comput.* (2021) doi:10.1162/neco_a_01342.

79. Izhikevich, E. M. Simple model of spiking neurons. *IEEE Transactions on Neural Networks* (2003) doi:10.1109/TNN.2003.820440.

789 **Supplementary material**

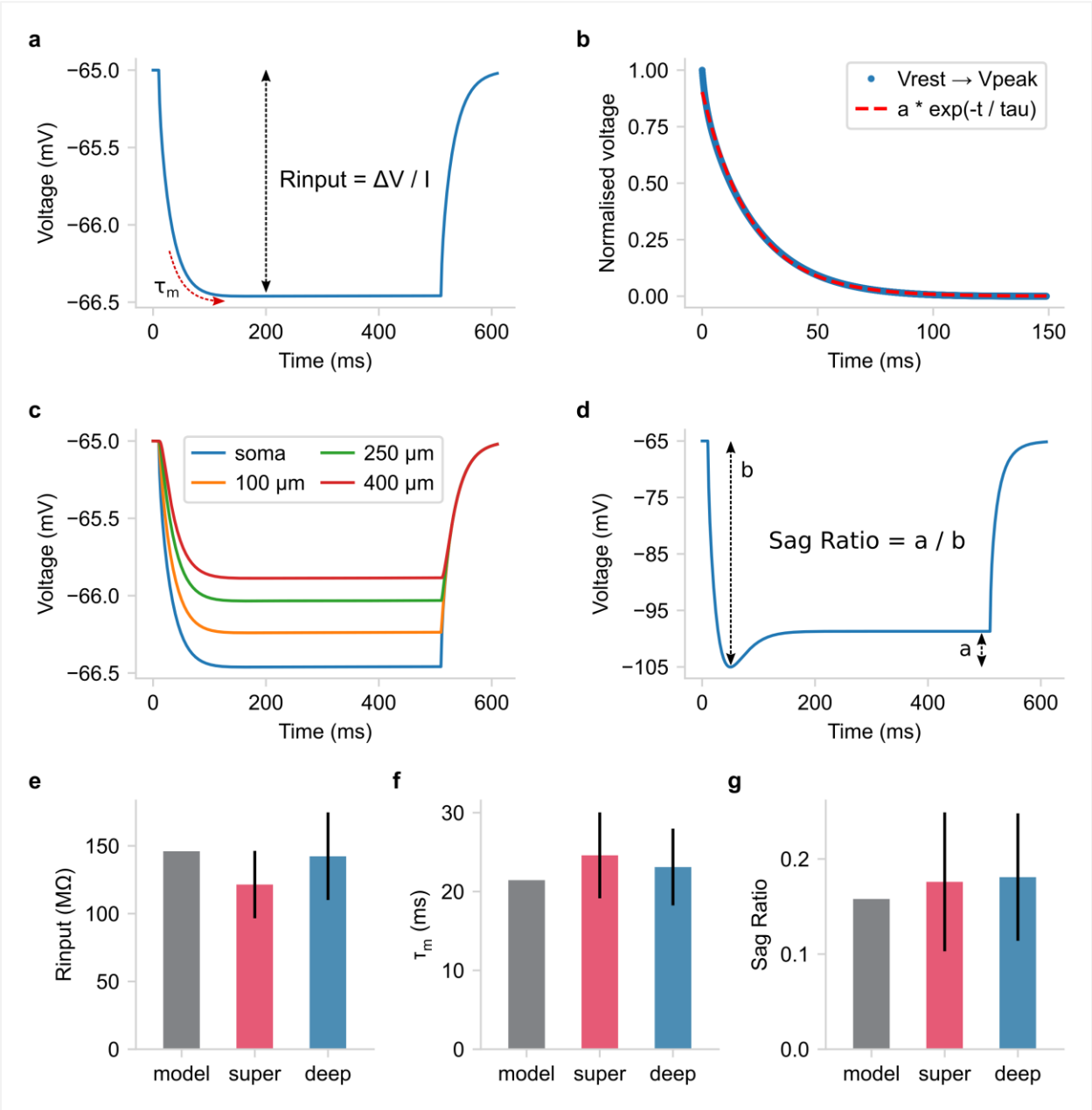

Figure S1 | Validation of the passive CA1 PC model properties (relevant to Fig. 6). a-c) Estimating various model properties by replicating an experimental[1], light somatic stimulation protocol (500 ms long somatic current injection of -10 pA amplitude). **a)** Schematic showing the somatic voltage trace used to calculate input resistance (R_{in}). **b)** The membrane time constant (τ_m) was measured by fitting a monoexponential to the somatic membrane hyperpolarization. **c)** Somatic

and dendritic voltage traces used to estimate the steady-state, distance-dependent voltage attenuation. **d)** Schematic showing the measurement of the sag ratio by using a strong somatic stimulation protocol[1] to elicit the sag response (500 ms long current injection of -394 pA amplitude to bring the somatic voltage to -105 mV). **e-g)** Comparing model properties against experimental *in vitro* data[1] regarding deep and superficial PCs of the CA1b Hippocampal region. The experimental values are depicted as means ± std (N_{super} = 29, N_{deep} = 27).

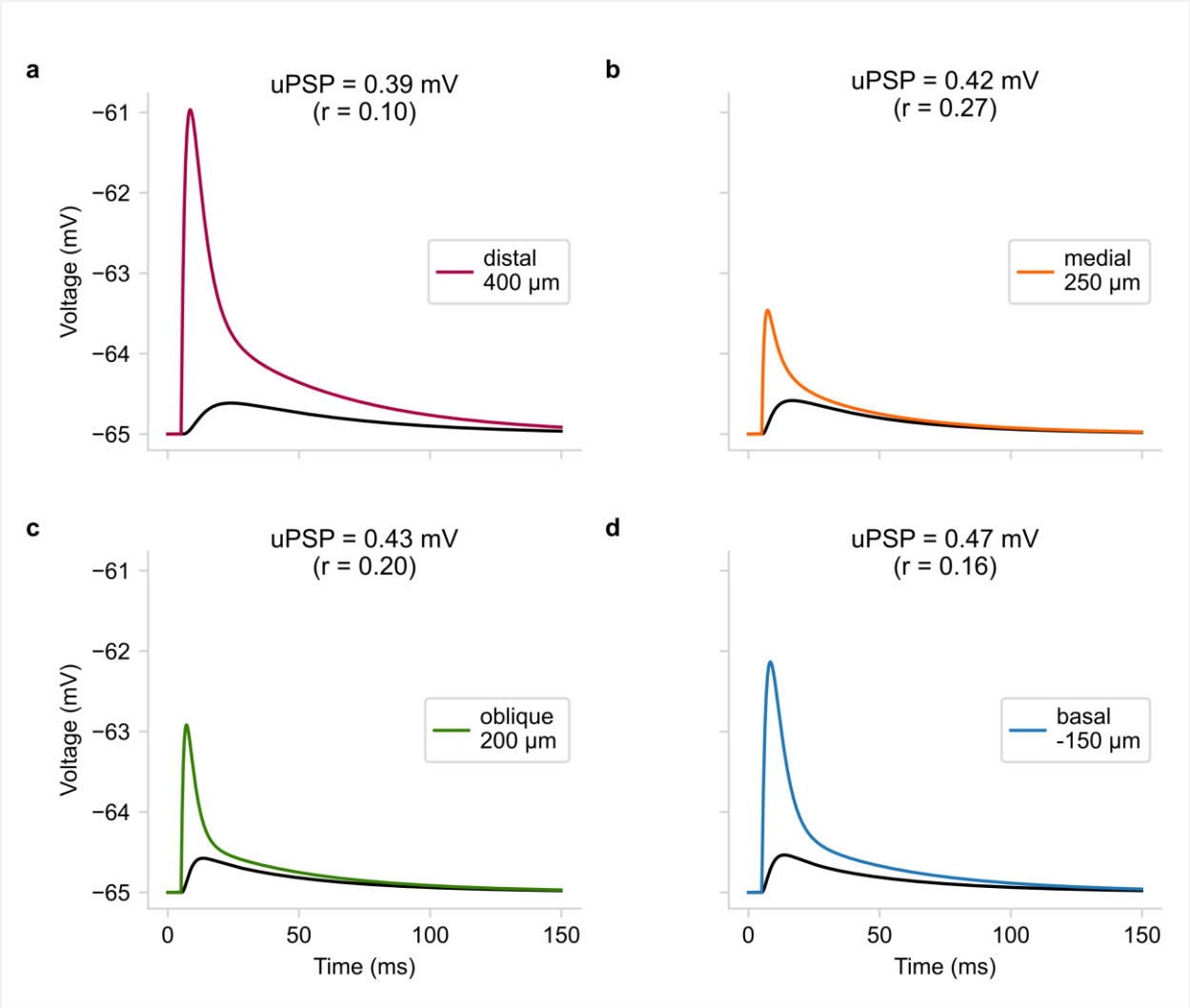

Figure S2 | Unitary synaptic responses of the CA1 PC model (relevant to Fig. 6). Overlay of the dendritic (colored) and the respective somatic (black) voltage responses when a single excitatory synapse is activated in each dendritic location. Synaptic conductances (g_{AMPA}, g_{NMDA}) were manually adjusted to achieve realistic somatic responses[2]. uPSP: somatic unitary postsynaptic potential. r: the ratio of the somatic to the dendritic peak voltage response ($\Delta V_{soma} / \Delta V_{dend}$).

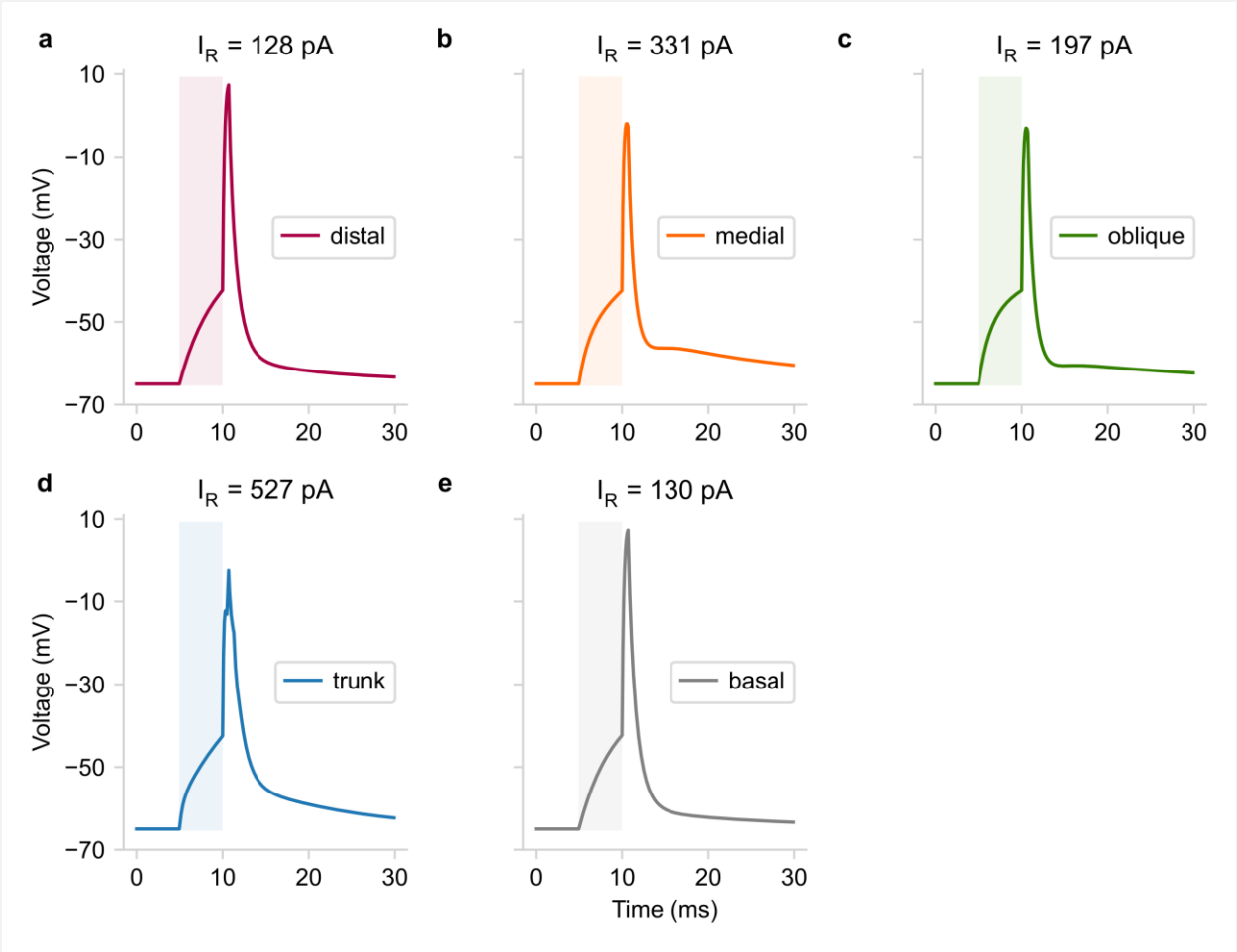

Figure S3 | Dendritic spiking in the CA1 PC model (relevant to Fig. 6). Dendritic voltage responses when Rheobase current (enough current to elicit a single dSpike) is injected directly into each dendrite (5 ms long square pulse). Notice that larger compartments such as the medial dendrite (**panel b**) and the trunk (**panel d**) require significantly more current (I_R) to generate a dSpike than smaller compartments. Shaded boxes: show the 5 ms long stimulation period. I_R: Rheobase (dSpike threshold) current.

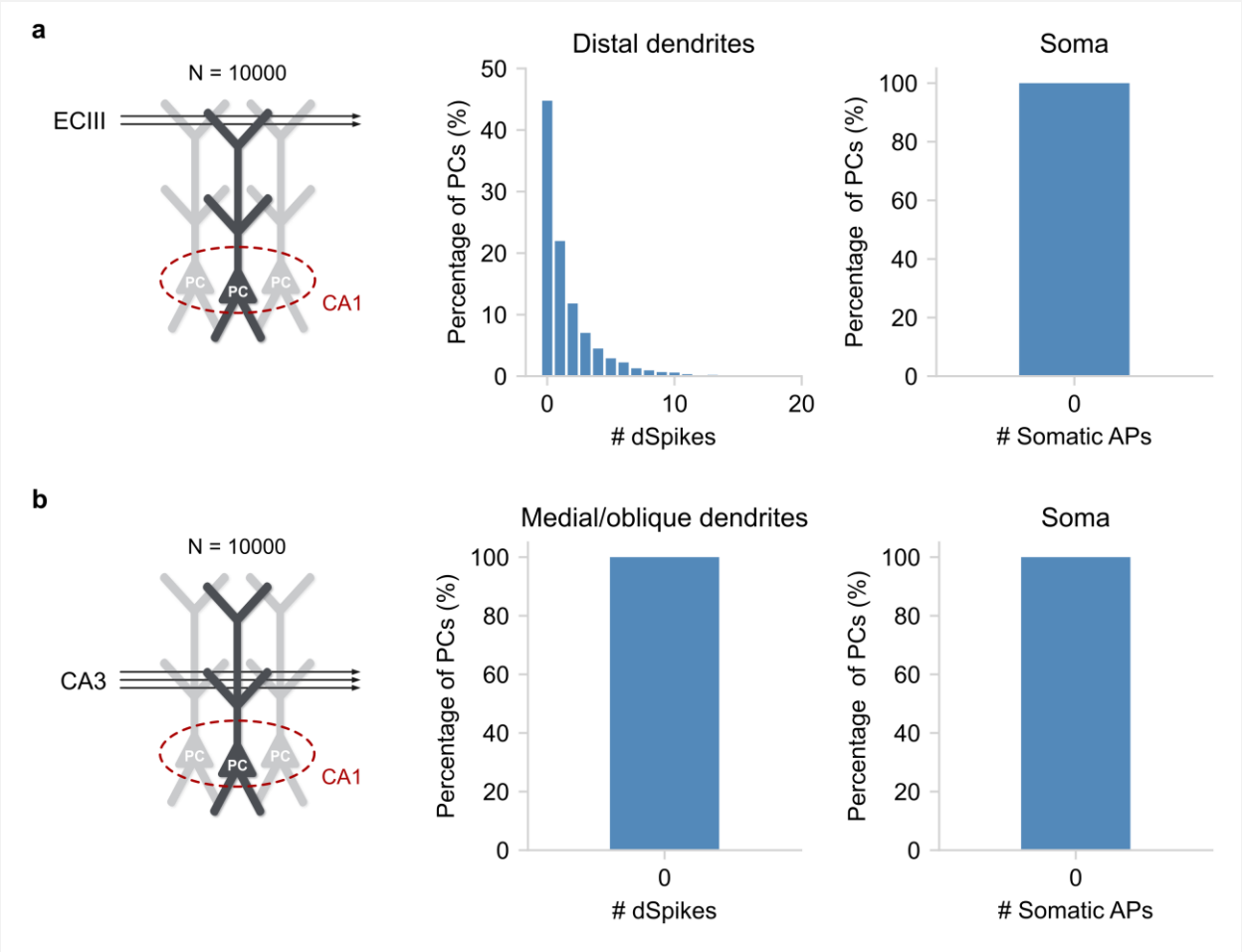

Figure S4 | Single pathway effect on somatic and dendritic spiking (relevant to Fig. 7). a) When only the ECIII input is administered to a pool of 10,000 PCs, more than half (~55%) will generate at least a single dSpike in one of their distal dendrites. However, due to strong dendritic attenuation, the effect on somatic output is negligible. **b)** When only the CA3 input is available, both the receiver dendrites (medial and oblique branches) and the soma produce subthreshold responses. Notably, both input pathways are simulated as independent Poisson processes, the rate of which is selected to mimic the experiments of Jarsky *et al.* [3].

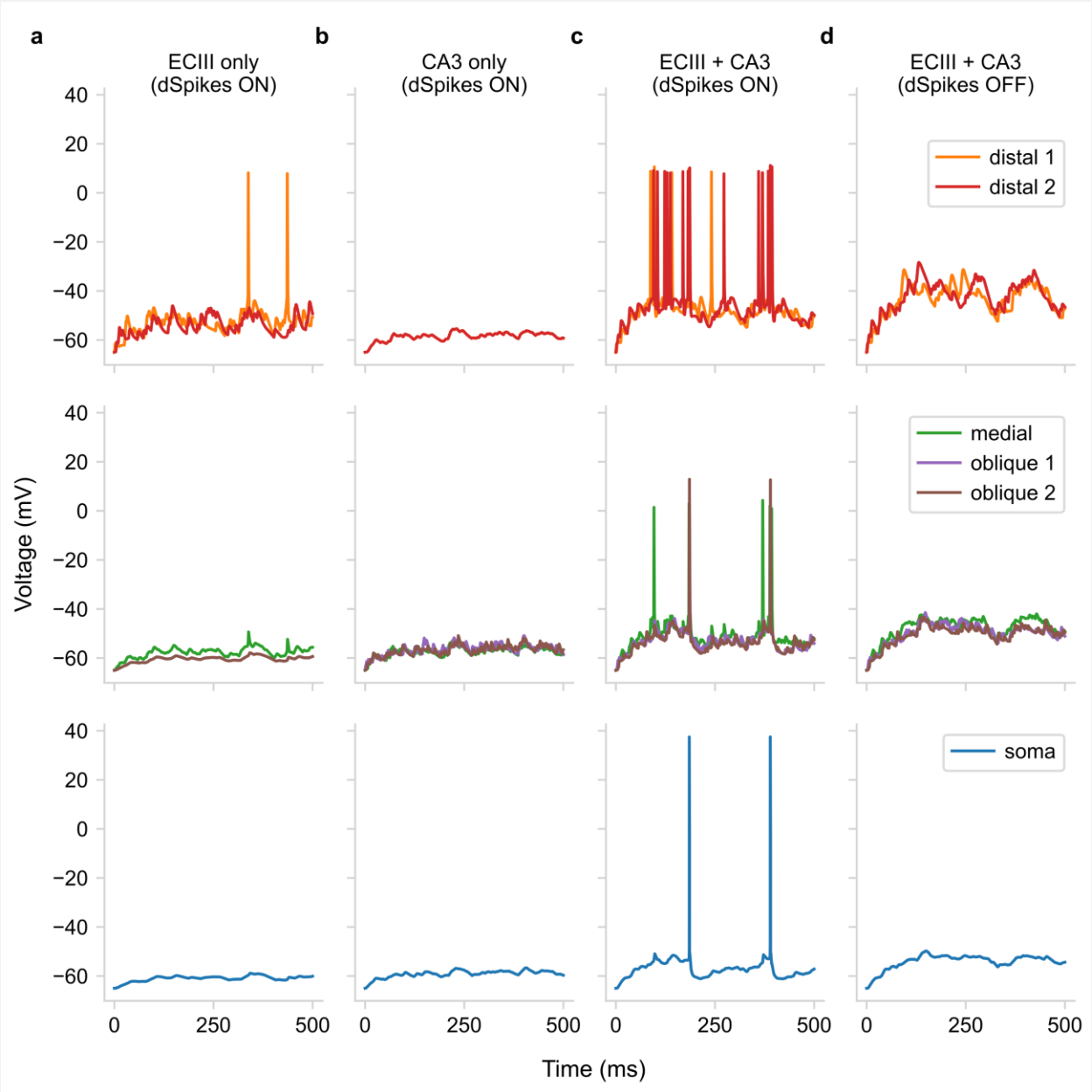

Figure S5 | Understanding the role of dendritic Na^+ spikes in coincidence detection in CA1 PCs (relevant to Fig. 7). a) When only the ECIII input pathway is active, distal dendrites can generate dSpikes that fail to propagate to the soma due to strong dendritic attenuation. **b)** When only the CA3 input pathway is active, it is not powerful enough to elicit any dendritic or somatic spikes. **c)** When both input the ECIII and CA3 pathways are active, their synergistic effect results in strong dendritic activation that succeeds in activating the soma. **d)** Deactivating dendritic spiking inhibits also deactivates the somatic output even when both input the ECIII and CA3 pathways are active.

Table S1 | Parameters for the model shown in Figure 2		
Timestep	dt	0.1 ms
Specific membrane capacitance	C_m	1 µF / cm^2
Specific leak conductance	g_L	50 µS / cm^2
Axial resistance	r_a	150 Ω · cm
Resting potential (all compartments)	V_{rest}	-70 mV
Spiking threshold	V_{th}	-40 mV
Voltage reset after spike	V_r	-50 mV
Refractory period after spike	t_{ref}	3 ms
Length soma	L_{soma}	25 µm
Diameter soma	D_{soma}	25 µm
Length apical	L_{apical}	250 µm
Diameter apical	D_{apical}	2 µm
Length basal	L_{basal}	150 µm
Diameter basal	D_{basal}	2 µm
Area scale factor	sf_{area}	3
Spine area factor	sf_{spines}	1.5
Coupling conductance (soma-apical)	$g_{soma \leftrightarrow apical}$	10 nS
Coupling conductance (soma-basal)	$g_{soma \leftrightarrow basal}$	10 nS
Noise mean intensity	μ_{noise}	0 pA
Noise standard deviation	σ_{noise}	3 pA
Noise time constant	τ_{noise}	20 ms
AMPA conductance	g_{AMPA}	1 nS
AMPA time constant	τ_{AMPA}	2 ms
NMDA conductance	g_{NMDA}	1 nS
NMDA time constant	τ_{NMDA}	60 ms
alpha (NMDA)	α	0.062 mV^{-1}
beta (NMDA)	β	3.57 mM
gamma (NMDA)	γ	0 mV
AMPA / NMDA reversal potential	E_{AMPA} / E_{NMDA}	0 mV

790

Table S2 | Parameters for the model shown in Figure 4		
Timestep	dt	0.1 ms
Specific membrane capacitance	C_m	1 µF / cm^2
Specific leak conductance	g_L	40 µS / cm^2
Axial resistance	r_a	150 Ω · cm
Resting potential (all compartments)	V_{rest}	-70 mV
Spiking threshold	V_{th}	-40 mV
1st voltage reset after spike	V_{r1}	40 mV
2nd voltage reset after spike	V_{r1}	-55 mV
Spike duration	d_{AP}	0.5 ms
Refractory period after spike	t_{ref}	5 ms
Length soma	L_{soma}	25 µm
Diameter soma	D_{soma}	25 µm
Length proximal	L_{prox}	100 µm
Diameter proximal	D_{prox}	2.5 µm
Length medial	L_{med}	100 µm
Diameter medial	D_{med}	1 µm
Length distal	L_{dist}	100 µm
Diameter distal	D_{dist}	0.5 µm
Area scale factor	sf_{area}	2.8
Spine area factor	sf_{spines}	1.5
Coupling conductance (soma-prox)	$g_{soma\leftrightarrow prox}$	15 nS
Coupling conductance (prox-med)	$g_{prox\leftrightarrow med}$	10 nS
Coupling conductance (med-dist)	$g_{med\leftrightarrow dist}$	4 nS
AMPA conductance	g_{AMPA}	0.8 nS
AMPA time constant	τ_{AMPA}	2 ms
NMDA conductance	g_{NMDA}	0.8 nS
NMDA time constant	τ_{NMDA}	60 ms
alpha (NMDA)	α	0.062 mV^{-1}
beta (NMDA)	β	3.57 mM
gamma (NMDA)	γ	0 mV
AMPA / NMDA reversal potential	E_{AMPA} / E_{NMDA}	0 mV
dSpike rise time constant	τ_{rise}	0.6 ms
dSpike fall time constant	τ_{decay}	1.2 ms
Refractory period after dSpike		5 ms
Offset of dSpike fall		0.2 ms

Table S3 | Parameters for the CA1 PC model shown in Figure 6		
Timestep	dt	0.1 ms
Specific membrane capacitance	C_m	1 µF / cm^2
Specific leak conductance	g_L	40 µS / cm^2
Axial resistance	r_a	120 Ω · cm
Resting potential (all compartments)	V_{rest}	-65 mV
Spiking threshold	V_{th}	-47.5 mV
Subthreshold adaptation activation voltage	V_a	-65 mV
Time constant of adaptation	τ_a	45 ms
Max subthreshold adaptation conductance	g_a	0.15 nS
Spike-triggered adaptation	Δg_α	21 nS
1st voltage reset after spike	V_{r1}	37.5 mV
2nd voltage reset after spike	V_{r1}	-53 mV
Spike duration	d_{AP}	0.8 ms
Refractory period after spike	t_{ref}	4 ms
Length soma	L_{soma}	30 µm
Diameter soma	D_{soma}	20 µm
Length trunk	L_{trunk}	100 µm
Diameter trunk	D_{trunk}	2 µm
Length medial	L_{med}	150 µm
Diameter medial	D_{med}	1.25 µm
Length distal	L_{dist}	150 µm
Diameter distal	D_{dist}	0.8 µm
Length oblique	L_{obl}	100 µm
Diameter oblique	D_{obl}	1 µm
Length basal	L_{bas}	150 µm
Diameter basal	D_{bas}	0.8 µm
Area scale factor	sf_{area}	2.9
Spine area factor	sf_{spines}	1.5
Coupling conductance (soma-basal)	$g_{soma\leftrightarrow basal}$	3.8 nS
Coupling conductance (prox-trunk)	$g_{prox\leftrightarrow trunk}$	22 nS
Coupling conductance* (trunk-oblique)	$g_{trunk\leftrightarrow obl}$	10.48 nS
Coupling conductance* (trunk-medial)	$g_{trunk\leftrightarrow med}$	10.82 nS
Coupling conductance* (medial-distal)	$g_{med\leftrightarrow dist}$	3.96 nS
AMPA reversal potential	E_{AMPA}	0 mV
AMPA time constant	τ_{AMPA}	2 ms
AMPA conductance distal	g_{AMPA_dist}	0.81 nS
AMPA conductance medial	g_{AMPA_med}	0.81 nS

AMPA conductance oblique	g_{AMPA_ob}	0.6 nS
AMPA conductance basal	g_{AMPA_bas}	0.6 nS
NMDA reversal potential	E_{NMDA}	0.35 mV
NMDA time constant	τ_{NMDA}	60 ms
NMDA conductance distal	g_{AMPA_dist}	0.81 nS
NMDA conductance medial	g_{AMPA_med}	0.4 nS
NMDA conductance oblique	g_{AMPA_ob}	0.4 nS
NMDA conductance basal	g_{AMPA_bas}	0.4 nS
Magnesium concentration	$[Mg^{2+}]_o$	1
alpha (NMDA)	α	0.087 mV^{-1}
beta (NMDA)	β	3.57 mM
gamma (NMDA)	γ	10 mV
Sodium reversal potential	E_{Na}	50 mV
Potassium reversal potential	E_K	-90 mV
dSpike threshold		-42.5 mV
dSpike rise time constant		0.5 ms
dSpike fall time constant		1.2 ms
Refractory period after dSpike		4.2 ms
Offset of dSpike fall		0.6 ms
Sodium channels conductance	g_{Na}	10 mS / cm^2
Potassium channels conductance	g_K	4 mS / cm^2

*Value generated by *Dendrify*

References

1. Masurkar, A. V. *et al.* Postsynaptic integrative properties of dorsal CA1 pyramidal neuron subpopulations. *J. Neurophysiol.* (2020) doi:10.1152/JN.00397.2019.

2. Golding, N. L., Mickus, T. J., Katz, Y., Kath, W. L. & Spruston, N. Factors mediating powerful voltage attenuation along CA1 pyramidal neuron dendrites. *J. Physiol.* (2005) doi:10.1113/jphysiol.2005.086793.

3. Jarsky, T., Roxin, A., Kath, W. L. & Spruston, N. Conditional dendritic spike propagation

following distal synaptic activation of hippocampal CA1 pyramidal neurons. *Nat. Neurosci.* (2005) doi:10.1038/nn1599.